nature communications

Article

https://doi.org/10.1038/s41467-025-57691-z

Pervasive impact modification of pristine lunar clasts

Received: 30 July 2024

Accepted: 28 February 2025

Published online: 13 March 2025

Check for updates

M. Barboni[1] ✉, E. Needham[1], D. Trail[2], E. A. Bell[3] & Hsin-Yu Chen[2]

Lunar rock fragments, particularly those deemed pristine, have long been considered vital records of the Moon's formation and magmatic evolution. These fragments were thought to have largely escaped the Moon's intense impact history, offering a window into the early lunar crust. However, the concept of "pristine" is increasingly debated, as traditional criteria for identifying pristine samples—based on texture, mineral content, and siderophile element abundances—may overlook the extensive effects of impact reworking. In this study, we apply a novel high-resolution geochemical and experimental approach, linking zircon Al content to parent melt composition, to critically assess lunar samples. Our findings reveal that clast zircons, assumed to preserve magmatic history, and matrix zircons, considered the last igneous remnants in brecciated samples, are not in chemical equilibrium with their surrounding glass. This disequilibrium, coupled with heterogeneous zircon ages, provides compelling evidence for pervasive impact reworking, challenging the assumption that these samples represent primary igneous lithologies. These results underscore the need for a serious re-evaluation of lunar materials. New analytical tools, tailored to each critical lunar lithology, will be essential for this reassessment—such as the Al-in-zircon method employed here for zircon-bearing samples.

Among the diverse array of lunar samples, those classified as pristine, particularly felsic clasts, have been considered essential records of the Moon's formation and magmatic history. These samples were believed to have remained relatively unaffected by the Moon's violent bombardment history and they therefore offered glimpses into the earliest lunar crust and the processes that shaped it[1–4]. Their unique geochemical signatures, mineral compositions, and ages have been interpreted as evidence of evolved magmatism on the early Moon[2,4–6]. Moreover, the concept of pristine igneous rocks has been fundamental to constraining the age of the Lunar Magma Ocean (LMO), the timing of magmatic differentiation, and the formation of the Moon itself[3]. However, defining pristine remains a contentious issue. While the Pristine Rock Concept[1,7–12] defines criteria for texture, siderophile element abundances, mineral content, sample size, chemical analysis, and petrologic diagrams to provide a framework for assessment, mounting evidence challenges this assumption of pristinity. Studies report shock metamorphism, compositional discrepancies, trace element heterogeneity, and age inconsistencies in both felsic and ferroan anorthosite (FAN) clasts[4,13–21], challenging their presumed pristine nature. This growing body of evidence suggests that lunar samples, although often interpreted as being of igneous origin, bear the marks of a more complex history involving impact-related characteristics. This controversy is not merely academic; it strikes at the heart of our understanding of lunar evolution. If even these seemingly pristine materials bear the marks of complex histories, our interpretations of the Moon's early development may require fundamental reassessment. Zircons play a crucial role in this pristinity debate as they are commonly used to date and characterize early lunar magmatic processes[13,22–25]. Their

[1]School of Earth and Space Exploration, Arizona State University, Tempe, AZ, USA. [2]Department of Earth and Environmental Sciences, University of Rochester, Rochester, NY, USA. [3]Department of Earth, Planetary, and Space Sciences, University of California Los Angeles, Los Angeles, CA, USA.
✉e-mail: mbarboni@asu.edu

robustness and ability to preserve primary magmatic signatures even under extreme conditions have made them key tools for reconstructing the Moon's early history. In lunar samples, zircons occur in various settings, including within impact melt breccias and evolved lithologies[2,13,22,24]. Among these, zircons in felsic clasts have been particularly important as they were traditionally interpreted as pristine igneous rocks preserving a direct record of evolved lunar magmatism[2,13]. Similarly, zircons found as isolated grains within breccia matrices were often viewed as fragments of broken pristine rocks[13,22,24]. However, the interpretation of these zircon records remains contentious. While some studies have documented clear shock deformation features in both clast and matrix zircons[15], many researchers maintain that these materials still preserve significant records of their primary igneous history, continuing to use them as benchmarks for lunar magmatism[13,22,24,26]. To resolve this fundamental question of preservation versus modification, we require new analytical approaches that can definitively distinguish between primary igneous signatures and impact-related alterations.

In this study, we focus on examining zircon grains and surrounding melt products within felsic clasts hosted in Apollo 14 and 17 breccias, as well as zircons found as isolated grains within the breccia matrix itself. Lunar impact breccias inherently contain materials from different sources due to their formation by impact events, providing a unique opportunity to explore the impact history recorded by these components. Our primary aim is to test the chemical equilibrium between zircon and coexisting melt products using Al-in-zircon partitioning, to determine whether these features truly represent a single, co-genetic assemblage or have been altered by post-crystallization processes. Building on the experimental work and observations of Wang et al. [27] and Trail et al. [28], we developed a methodology that links Al content in zircon to lunar melt composition, enabling us to evaluate the genetic relationships between zircons and their associated glasses. Our analyses reveal pervasive chemical disequilibrium between zircons and their surrounding glass phases, coupled with heterogeneous zircon ages and compositions within individual clasts. By directly comparing the Al content in zircon to that of the surrounding melt products, we document extensive impact modification and challenge the assumption that these materials reliably represent primary igneous lithologies. This has significant implications for our understanding of lunar magmatic evolution and the extent of impact modification in rocks previously considered pristine.

Results

Experimental design and analytical framework

We conducted a multi-faceted analytical study to assess the chemical equilibrium between zircon and coexisting melt in lunar breccia samples. We identified 196 lunar zircons from 11 Apollo sample thin sections using EDS and WDS mapping. We then documented samples with BSE imaging for texture, inclusion, and surrounding phase characterization. We applied strict filtering criteria based on zircon size—i.e., large enough to accommodate two clean ion microprobe spots to quantify Pb-Pb age and Al concentration – and proximity to glass. This yielded a subset of 14 lunar zircons from 6 thin sections (12013,7; 14303,49; 73235,59; 73235,60; 73217,15; 73217,52) for in-depth analysis (Data S1; Figs. 1 and 2; Figs. S1–S7; see Methods for additional details on the selection process). Our selection consists of zircons hosted in two felsic clasts previously deemed pristine based on textural, mineralogical, and chemical criteria (14303,49 and 73235,60[1,2]), and zircons found as isolated grains within the breccia matrix. All selected zircons were analyzed for Pb-Pb age determination (complemented by literature ages obtained on the same grains), Al content, Ti content (for crystallization temperature estimation), and select trace elements using Secondary Ion Mass Spectrometry (SIMS; Data S2; see Methods). Complementary electron probe microanalysis (EPMA) was conducted on glass inclusions within the zircons, glass in contact with the zircons, and glass near the zircons (Fig. S8; Data S1–S4; see Methods).

To link the zircon parent melt to the melt composition(s) recorded by the glass inclusions and adjacent glass, experimental work was conducted to crystallize synthetic zircons under reduced lunar conditions and to calibrate the relationship between Al content in zircon and melt composition. These experiments were performed across a temperature range of 1050–1300 °C (Fig. S11) and a pressure of 1 GPa and 1 atm using five distinct melt compositions that capture a broad spectrum of lunar magmatic processes, including KREEP basalt, granitic melts, quartz monzodiorite, highland basalt mixtures, and monzonite (Methods and Data S5). These compositions were specifically chosen to reflect the diversity of lunar melt evolution, encompassing both primary magmatic products and secondary processes linked to impact reworking. Our rationale for selecting these compositions was to explore the full range of plausible Al_2O_3 and SiO_2 concentrations that could influence zircon crystallization on the Moon. The experiments were water-bearing (~3 wt% H_2O). Our decision to include water in the experimental setup was driven by the observation that Al^{3+} incorporation into zircon can be facilitated through H^+ charge balancing[29], as well as its ability to depolymerize silicate melts, enhancing Zr diffusivity and enabling the growth of analyzable zircon crystals within laboratory timescales. While we acknowledge that not all lunar lithologies contain significant water, studies like Simon et al. [30] have shown that water content in lunar felsites can vary widely depending on factors such as shock history and impactor material. To test the influence of water, we also conducted anhydrous experiments at 1 atm and 1200 and 1250 °C, which revealed no significant differences in zircon-melt Al partitioning compared to the water-bearing runs (Methods). This suggests that the presence of water does not fundamentally alter the zircon-melt equilibrium, reinforcing our decision to include it in most experiments to ensure a broader exploration of melt conditions.

From first principles, we predict that Al incorporation in zircon will be proportional to Al availability in the parent magma. While previous studies of terrestrial zircons found that the aluminum saturation index (ASI; $Al_2O_3/[CaO+Na_2O+K_2O]$) of the silicate melt best correlated with zircon Al content[27,28], our experiments on lunar compositions reveal that this relationship needs modification for lunar silicate systems. For the terrestrial studies, all had relatively consistent SiO_2 content, and so the silica variation did not significantly impact the Al-incorporation model. However, lunar magmas show substantial SiO_2 variability, requiring us to account for its influence. Our results from 40 experiments demonstrate that the strongest correlation between zircon and melt Al content is achieved using the parameter $(Al_2O_3)^{0.5}/SiO_2$ (by mole; Fig. S9). For glass samples, whether lunar or experimental, we measure this parameter directly and refer to it as AlI_{glass}. Using our experimental calibration of Al content in zircons grown from melts of known composition, we can also calculate the expected $(Al_2O_3)^{0.5}/SiO_2$ ratio of a zircon's parent melt, which we term AlI_{zpm}. To facilitate reproducibility, Data S8 provides a tool for automatically calculating AlI_{zpm} and AlI_{glass} from the measured glass wt.% values of Al_2O_3 and SiO_2, along with Al-in-zircon concentrations. In a cogenetic scenario where zircon crystallizes from its parent melt, we expect a positive correlation between AlI_{zpm} and AlI_{glass}, even if their absolute values do not match perfectly due to variations in partitioning behavior and crystallization conditions. This positive correlation serves as the key diagnostic feature of equilibrium crystallization. While direct correlation testing is most powerful when multiple measurements are available for individual zircons, many grains preserve only a single Al measurement. In these cases, we adopt a broader correlation approach by plotting all matrix zircons together to examine the overall relationship between zircon and glass compositions in the sample. Although multiple zircon and glass generations may be

https://doi.org/10.1038/s41467-025-57691-z

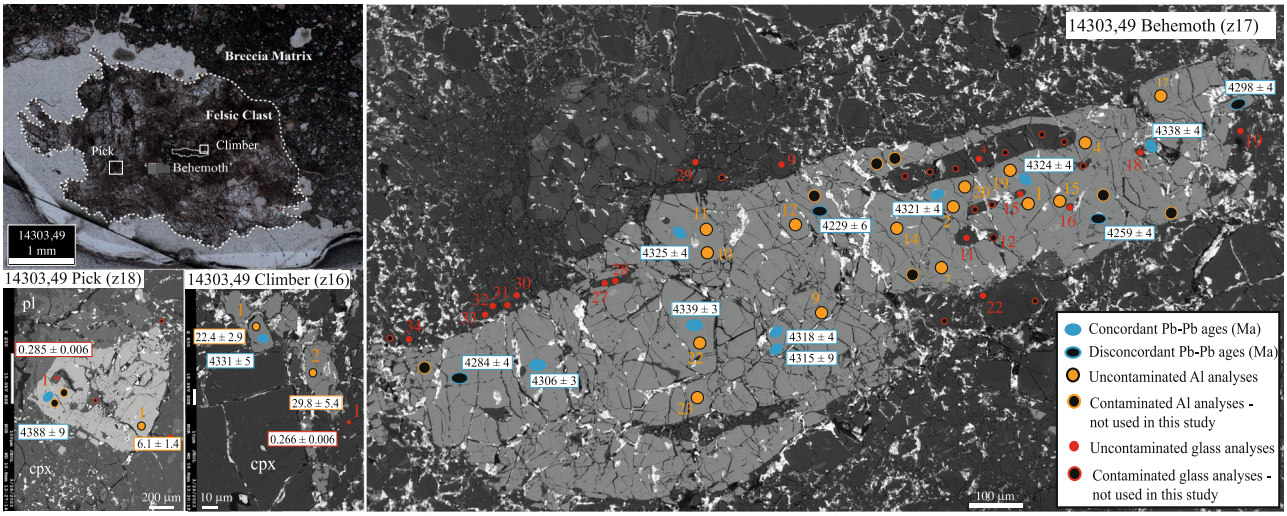

14303,49 Z17 - Behemoth

Al-in-zircon					*Al-in-glass*		
Spot #	Al ppm	1σ	AlI_{zpm}*	1σ	Spot #	AlI_{glass}	1σ
1	19.5	6.7	0.033	0.003	4	0.29	0.01
2	3.8	0.7	0.007	0.001	9	0.30	0.01
4	10.8	1.4	0.018	0.002	11	0.29	0.01
7	7.9	1.4	0.014	0.001	15	0.30	0.01
9	26.3	6.1	0.045	0.004	16	0.30	0.01
10	7.8	1.1	0.013	0.001	18	0.30	0.01
11	3.4	0.5	0.006	0.001	19	0.28	0.01
12	4.5	0.7	0.008	0.001	22	0.28	0.01
14	5.4	1.3	0.009	0.001	27	0.29	0.01
15	5.4	0.9	0.009	0.001	28	0.29	0.01
17	38.3	7.0	0.066	0.007	29	0.30	0.01
19	3.2	0.4	0.005	0.001	30	0.28	0.01
20	3.5	0.5	0.006	0.001	31	0.28	0.01
22	3.3	0.4	0.006	0.001	32	0.28	0.01
					33	0.28	0.01
					35	0.27	0.01

* Forced through origin

Fig. 1 | Zircons in the felsic clast hosted in sample 14303,49. Back-scattered electron (BSE) images of zircons Behemoth, Pick, and Climber, with Pb-Pb age (blue circle with blue rims are concordant; black circles with blue rims are discordant and not used in this study), Al-in-zircon (orange circles and rims are uncontaminated, black circle with orange rims are contaminated and not used in this study), and glass analysis (red circles and rims are uncontaminated, black circle with red rims are contaminated and not used in this study) locations. Actual values for Behemoth indicated in Table. The oldest, concordant regions of Behemoth exhibit two distinct parent magma compositions (Al-in-zircon content of <10 ppm and >20 ppm) with similar ~4.33 Ga ages, suggesting multiple magmatic events in a short time span. The younger, texturally distinct rim of Behemoth yields a ~ 4.2 Ga age, interpreted as impact-related. Pick and Climber each record one of the two old magma compositions observed in Behemoth. The striking discrepancy between the Al content of the clast glass and the zircon parent magmas provides compelling evidence that the 14303 clast is a polymictic breccia rather than a pristine igneous rock. Uncertainties are reported as 1σ.

present, if equilibrium conditions dominate, we should still observe an overall positive correlation. For individual zircon-glass pairs, we also employ an experimentally derived ratio benchmark. Our controlled equilibrium experiments established that AlI_{zpm}/AlI_{glass} ratios consistently fall between 0.37 and 1.98 (mean ~1.28) in cogenetic zircon-glass pairs. This provides a quantitative framework for assessing equilibrium: while small deviations from this range may reflect natural partitioning effects, large deviations indicate disequilibrium and suggest the surrounding glass is not the parent melt from which the zircon crystallized.

Our approach specifically acknowledges the brecciated nature of lunar samples, understanding that this mixture of materials from diverse sources naturally results in variability in aluminum content across the breccia matrix. However, by focusing on zircon-bearing components, our Al-in-zircon partitioning method probes localized chemical equilibria with coexisting melt products. This targeted approach allows us to investigate magmatic interactions at the sub-grain level within individual zircon grains, even in a complex brecciated environment. This capability is crucial for identifying fine-scale chemical signals that might otherwise be masked by the overall heterogeneity of the breccia. The observed chemical disequilibrium between the zircon, surrounding glass, and glass inclusions strongly supports the interpretation that these features were affected by post-crystallization impact processes. This interpretation aligns with findings from studies like Crow et al. [31], which have shown that impact melts exhibit distinct chemical characteristics compared to other lunar lithologies. Our approach enables the isolation and characterization of specific zircon-melt interactions, providing valuable insights into both the conditions of crystallization and subsequent impact reworking. While brecciated systems are inherently complex, our method offers a rigorous way to test these relationships and supports the need to develop additional tools for understanding the chemical evolution of these intricate lunar samples.

Zircon-melt disequilibrium in lunar clasts

The zircon ages range from 4017 ± 12 to 4405 ± 22 Ma (1σ; Figs. 1 and 2; Data S2) and exhibit Al contents primarily below 20 ppm (average of 12 ± 2 ppm; 1σ), with one analysis reaching up to 46 ± 6 ppm (1σ;

https://doi.org/10.1038/s41467-025-57691-z

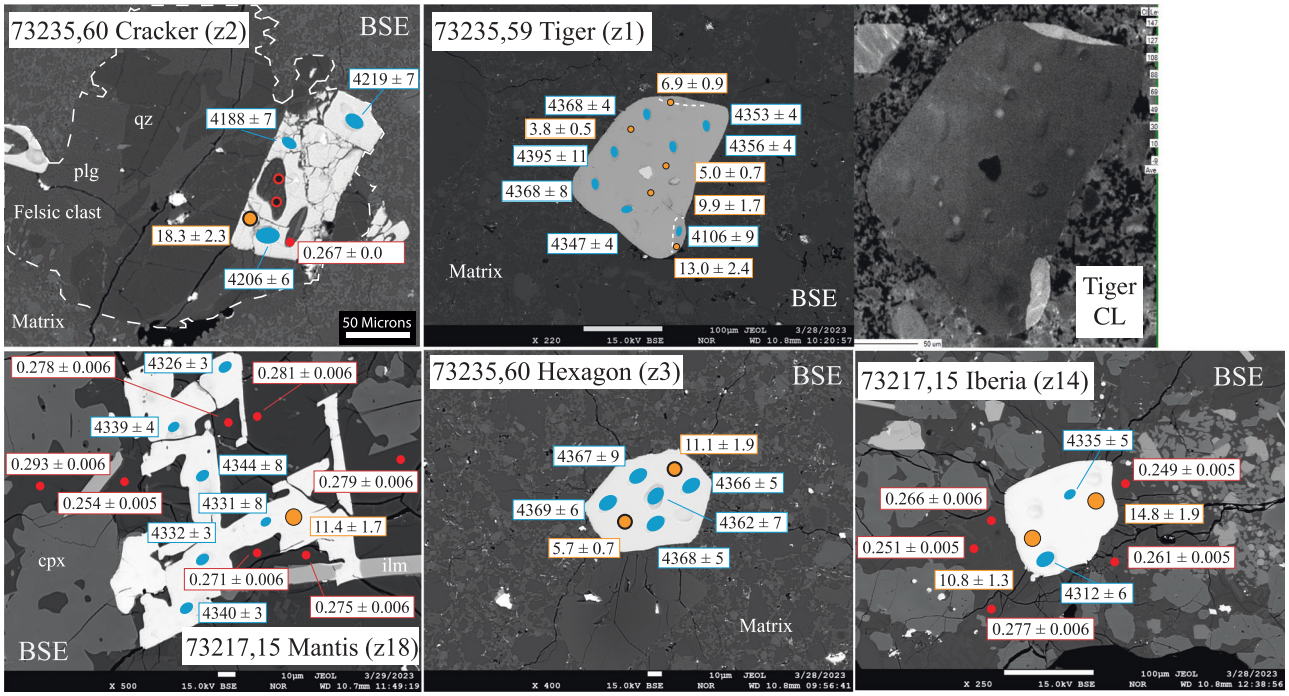

Fig. 2 | Representative zircon in samples 73235,60, 73235,59, and 73217. BSE images of zircons (plus CL for the zircon Tiger), with Pb-Pb age (Ma; blue circles), Al-in-zircon content (ppm; orange circles), and glass analysis (red circles for uncontaminated analyses, black circles with red rims for contaminated analyses not used in this study) locations and values indicated. Cracker is hosted in a felsic clast, while all other zircons are found in the brecciated matrix. Tiger displays distinct Al contents in its old core and young, recrystallized rim, validating Al as a tool to decipher different parent magmas within a single grain. Hexagon and the pristine part of Tiger exhibit similar ages and textures but distinct Al contents, suggesting a more complex origin than simple igneous crystallization. See Methods for additional matrix zircons mentioned in the text. Uncertainties are reported as 1σ.

Data S2). We apply our experimental results to calculate Al_{zpm}, which range from 0.005 ± 0.001 to 0.079 ± 0.008 (1σ; Data S2). We conducted over 100 lunar glass analyses by EPMA and obtained 38 uncontaminated glass analyses suitable for this study, including 8 zircon inclusions, 28 touching zircons, and 2 within 100 µm of the grains but not touching (Data S1). The glasses have high SiO_2 (70 to 79 wt%), Al_2O_3 (11 to 14 wt%) and K_2O (7 to 11 wt%) corresponding to $(Al_2O_3)^{0.5}/SiO_2$ ratio (Al_{glass}) ranging from 0.25 ± 0.01 to 0.30 ± 0.01 (1σ; Data S3). When plotting Al_{zpm} against Al_{glass}, we observe a flat to slightly negative trend (Fig. 3A, B). In a cogenetic scenario, we would expect a positive correlation between these parameters, as higher Al content in the parent melt should result in higher Al content in the crystallizing zircon. The absence of this positive correlation indicates that, in aggregate, the zircons and glass do not share a common origin. These zircons align with the previously documented low Al population of Apollo 14 zircons[32] (Fig. S10). The glass compositions in our study closely resemble those reported by Crow et al. [31] for zircon-hosted melt inclusions in the Apollo 14 impact melt breccia 14311 (Fig. 4). These inclusions were interpreted as products of localized shock melting of feldspar and quartz during impact events, drawing parallels with K-Al-Si-rich eutectic-like melts observed in zircons from the terrestrial Vredefort impact structure[33]. The consistency of glass compositions across our samples, including both inclusions and glasses adjacent to zircon grains, coupled with their marked deviation from typical lunar lithologies, strongly suggests that impact processes played a significant role in their formation. However, the glass inclusions in our study are often substantially larger than the micron to submicron ovoid blebs analyzed by Crow et al.[31] especially those fully enclosed within the zircon interiors. The zircon-melt chemical disequilibrium, as indicated by the contrasting Al_{zpm} and Al_{glass}, extends to these larger, primary-appearing melt inclusions. This suggests that impact-related processes were more pervasive than previously recognized, affecting not only small shock melt blebs along fractures but also larger melt inclusions. Further studies of glass in lunar samples associated with impact features could clarify whether Crow's[31] findings of small impact blebs are consistent across other samples, and whether larger glass inclusions, such as those observed in our study, are more widespread. Finally, while the observed Al heterogeneity in the zircons may hint at traces of earlier evolved magmatic processes, the strong chemical disequilibrium between the zircon grains and their surrounding glass phases suggests that impact-related reworking is the dominant process responsible for these features. The presence of large glass inclusions within the zircon interiors, coupled with their deviation from typical lunar lithologies, supports the conclusion that impact processes likely overprinted any earlier magmatic signatures. These complexities highlight the dual nature of the zircon record, where both magmatic and impact processes contributed to the observed geochemical signatures, but the pervasive influence of impacts remains the most compelling explanation.

Challenging the pristine nature of felsic clast 14303

The prevailing paradigm of pristine lunar clasts, exemplified by interpretations of the 14303 felsic clast[2,13], is directly challenged by our Al-in-zircon data. While previous studies, such as Zhang et al. [34] have raised questions about the provenance of zircons and impactites, our results provide clear evidence of pervasive impact reworking. We show that, rather than a simple igneous history, the 14303 clast records multiple magmatic events and significant impact modification. The Behemoth zircon (reported as 14303,49 zircon#1 in ref. 13) despite exhibiting concordant domains with a ~4.33 Ga age, preserves evidence for two distinct parent magma compositions (<10 ppm and >20 ppm Al; Figs. 1, 3, 5), requiring a rapid succession of magmatic pulses not easily reconciled with existing models of pristine clast formation. Furthermore, the presence of a younger, texturally distinct rim on Behemoth (~4.2 Ga, interpreted as impact-related by Grange et al. [13]) demonstrates that at least three distinct magmatic episodes

https://doi.org/10.1038/s41467-025-57691-z

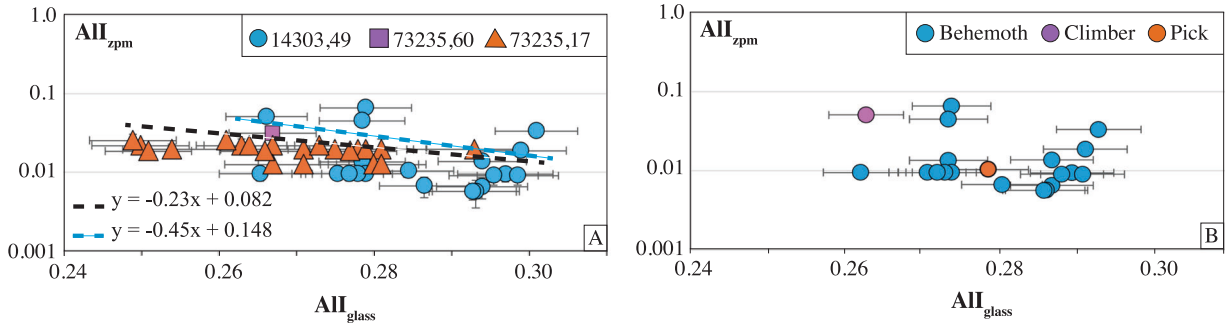

Fig. 3 | Al_{lass} vs AlI_{zpm} for zircons and coexisting glass. A All zircon and glass data, showing a flat to negative correlation, as indicated by the linear regression equation (whole data set in black; only Behemoth zircon analyses in blue). Orange triangle are matrix zircons from 73235,17, purple squares are matrix zircons from 73235,60 and blue circles are felsic clast zircons from 14303,49. **B** Zircon and glass data from sample 14303,49, including Behemoth (blue circle), Pick (orange circles, and Climber (purple circles), also exhibiting a flat to negative correlation. A positive correlation would be expected if the zircon and melt were cogenetic, suggesting that the zircons and glass do not share a common origin. Error bars show 1σ uncertainties.

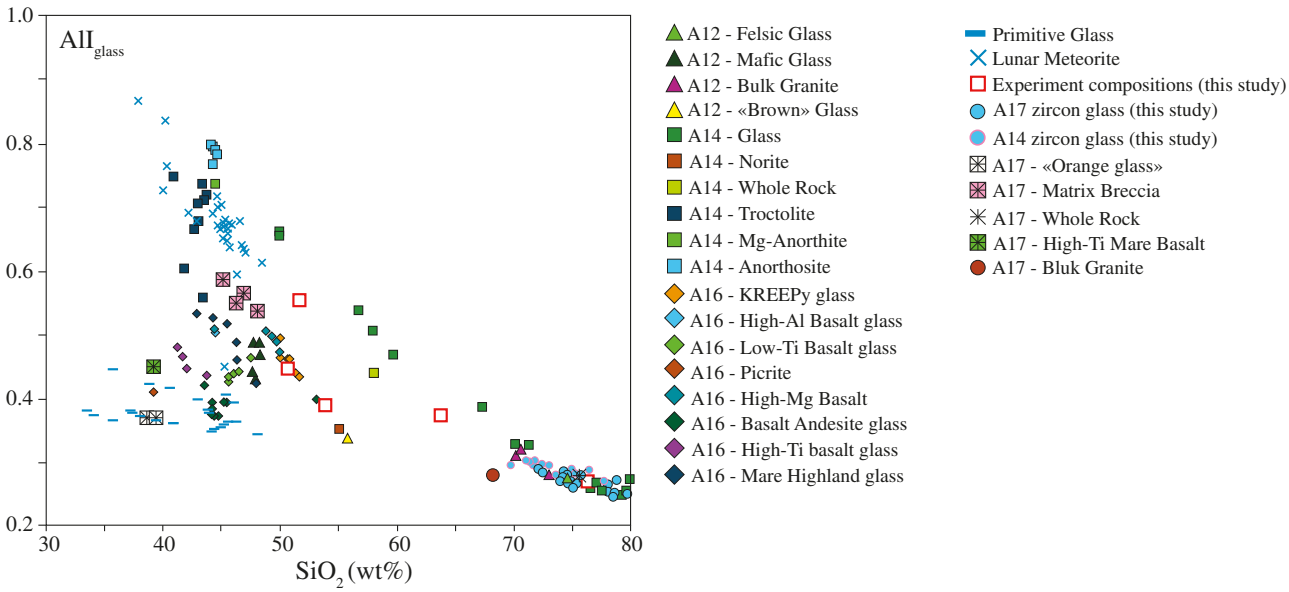

Fig. 4 | Comparison of glass data from this study with literature data. Plot of AlI_{glass} versus SiO_2 (wt%). Symbols: filled green triangles−A12 felsic glass (Ref. 4); filled dark green triangles−A12 mafic glass (Ref. 6); filled magenta triangles−A12 bulk granite (Ref. 66); filled yellow triangles−A12 brown glass (Ref. 67); filled green squares−A14 glass (Ref. 31); filled brown squares−A14 norite (Ref. 67); filled yellow-green squares−A14 whole rock (Ref 67.; filled dark green squares−A14 troctolite (Ref. 68); filled lime squares−A14 Mg-anorthosite (Ref 68); filled blue squares−A14 anorthosite (Ref. 68); filled orange diamonds−A16 KREEP basalt (Ref. 69); filled light blue diamonds−A16 high-Al basalt (Ref. 69); filled green diamonds−A16 low-Ti basalt (Ref. 69); filled brown diamonds−A16 picrite (Ref. 69); filled blue diamonds−A16 high-Mg basalt (Ref. 69); filled dark green diamonds−A16 basalt andesite (Ref. 69); filled violet diamonds−A16 high-Ti basalt (Ref. 69); filled navy diamonds−A16 mare highland (Ref. 69); blue lines - primitive glass (Ref. 70); blue crosses−lunar meteorite (Ref. 70); open red squares−experimental compositions (this study); blue circles−A17 zircon glass (this study); blue circles with pink rims−A14 zircon glass (this study); hatched grey squares−A17 orange glass (Ref. 71); hatched pink squares−A17 matrix breccia (Refs. 72); complex black crosses−A17 whole rock (Ref. 67); green squares with complex crosses−A17 high-Ti mare basalt (Ref. 71); filled brown circles - A17 bulk granite (Ref. 66); Our analyzed glasses cluster at high SiO2 (>70 wt%) within the field defined by Crow et al. [31] for impact melts from Apollo 14 breccia 14311, distinct from typical lunar magmatic compositions. This compositional similarity suggests that impact processes played a significant role in forming the glass associated with our studied zircons.

are recorded within this single grain. An alternative explanation for the observed age variability is the possibility of Pb-loss due to the impact-affected nature of these zircons. If Pb were to diffuse away, Al might similarly have diffused during post-crystallization disturbances. However, Grange et al.[13] evaluated Pb-loss in the "Behemoth" and concluded that while Pb diffusion may occur via impact-induced fractures, this alone could not explain the full extent of age variations. This supports our interpretation that the observed ages represent distinct magmatic episodes rather than solely being the result of Pb-loss. Precisely quantifying Pb-loss through SIMS is not feasible and would require high-precision techniques like TIMS[35]. Additionally, no clear correlation between Al and Pb diffusion has been established. While future studies may further clarify Pb-loss and its relation to the diffusion of other elements, the current evidence supports our conclusion of multiple crystallization events. This complex history is corroborated by zircons Pick and Climber (Figs. 1 and 5), each exhibiting one of the two older zircon compositions observed in Behemoth. Most significantly, we find that the glass compositions within the 14303 clast do not positively correlate with the inferred zircon parent magma compositions (Fig. 3). This crucial observation, coupled with the striking similarity between the 14303 glass and impact melts reported in Apollo 14 breccia 14311[31], compels a reinterpretation of the 14303 clast as a

https://doi.org/10.1038/s41467-025-57691-z

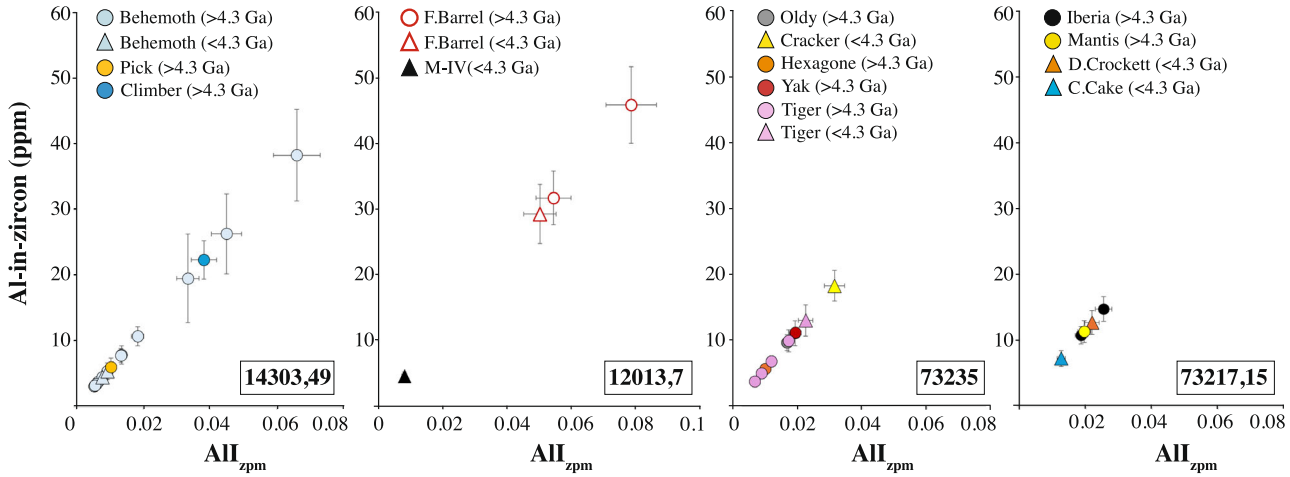

Fig. 5 | Al-in-zircon vs. All_{zpm} for all studied zircons. This figure illustrates how individual zircons record distinct parent melt compositions, sometimes even within a single grain, and how zircons from the same sample capture either similar or different magmatic histories. The Behemoth zircon records two distinct magma compositions in its oldest domains, while the Pick and Climber zircons each record one of these compositions. This figure illustrates how individual zircons record distinct parent melt compositions, sometimes even within a single grain, and how zircons from the same sample capture either similar or different magmatic histories. Sample 14303,49: light blue circles—Behemoth (> 4.3 Ga); light blue triangles—Behemoth (< 4.3 Ga); orange circles—Pick; blue circles—Climber. Sample 12013,7: Open red circles—Faulted Barrel (> 4.3 Ga); Open red triangles—Faulted Barrel (< 4.3 Ga); black triangles—Mark IV. Sample 73235: gray circles—Oldy; yellow triangle—Cracker; orange circles - Hexagon; red circles—Yak; pink circles—Tiger Faulted Barrel (> 4.3 Ga); pink triangles—Tiger Faulted Barrel (> 4.3 Ga). Sample 73217,15: black circles - Iberia; yellow circles—Mantis; orange triangle—Davy Crockett; blue triangle—Crumble Cake. Error bars show 1σ uncertainties.

polymict breccia assembled through a combination of magmatic and impact processes.

Complex impact histories recorded in matrix zircons

The matrix zircons in brecciated samples 73235 and 73217 display a wide range of All_{zpm} values and ages, indicating crystallization in diverse magmatic environments prior to their incorporation into the breccia (Figs. 2 and 5; Methods). These zircons have been interpreted as either relics of minerals separated from felsic clasts, potentially characterizing endogenic processes, or as impact-related grains providing insights into impact geochronology, based primarily on age and texture relationships[13,22,24–26,36]. Grange et al. [13] demonstrated the utility of this approach in sample 73235 for the matrix zircon Tiger (also reported as 73235-59#3 in refs. 13,22), which displays a recrystallized rim with younger ages and different trace element concentrations, including Th/U ratios, compared to the core (Fig. 2). Our Al analysis of the old core and young rim of Tiger corroborates their findings, revealing distinctly higher Al (13 ppm) in the recrystallized zone compared to the pristine zone (avg. 6 ppm; Fig. 5), validating Al as a tool to decipher different parent magmas within a single grain and confirming our conclusions for the composite Behemoth grain in felsic clast 14303.

While the Grange et al. [13,22] approach successfully identifies the two distinct zones in Tiger based on age, texture, and Th/U ratios, it appears to be limited when applied to apparently homogeneous growth zones. The pristine core of Tiger and the Hexagon (also reported as 73235-60#4 in ref. 22) zircon, interpreted as single growth events by Grange et al. [22] based on their uniform age, texture, and Th/U ratios, and further supported by our own analyses of Th/U, Y, and Hf (Data S2), actually exhibit distinct Al contents (Figs. 2 and 5; Methods). This suggests that these seemingly homogeneous zones are the result of multiple magmatic events, a complexity not captured by the other criteria. Importantly, the observed chemical disequilibrium between matrix zircons and their surrounding phases is interpreted as evidence of genuine post-crystallization modifications, rather than being an inherent consequence of analyzing isolated grains from the breccia matrix. The All_{zpm} variations across these matrix zircons suggest significant reworking, likely due to impact events, challenging the assumption that these grains retain pristine igneous signature. When examining the collective dataset of matrix zircons to test for broader equilibrium patterns, we observe a flat to negative trend between All_{zpm} and All_{glass} (Fig. 3B), providing sample-wide evidence that impact-driven processes have disrupted the primary melt-zircon equilibrium. In addition to the complexities revealed in these matrix zircons, the felsic clast-attached zircon Cracker in 73235 (reported as 73235-60#5 in ref. 22) also exhibits a higher Al content (18 ppm; Fig. 2) than the matrix zircons, reminiscent of 14303 clast compositions but with a younger age (ca. 4.2 Ga; Fig. 2). The All_{zpm}/All_{glass} ratio for Cracker is 0.11 (Data S6), significantly lower than the experimentally constrained equilibrium range (0.37–1.98, mean ~1.28; Data S7), suggesting that the zircon and surrounding glass are in disequilibrium. The composition of the glass itself, enriched in both SiO_2 and Al_2O_3 and with an All_{glass} of 0.27, closely matches previously identified impact melts in similar samples (Fig. 4), suggesting an impact origin for the glass[31].

Similarly, the matrix zircons in sample 73217 record a complex impact history rather than simple endogenic processes. The Mantis zircon, interpreted as impact-recrystallized at ca. 4.33 Ga based on its acicular morphology and ilmenite association, was thought to have crystallized from the surrounding felsic impact melt[24]. However, our Al data challenge this assumption: the All_{zpm}/All_{glass} ratio for Mantis (0.066–0.071) is well below the experimentally constrained equilibrium range, demonstrating disequilibrium with the surrounding glass. Given that the glass composition closely resembles impact-generated melts[31], it is unlikely that Mantis crystallized from it, instead originating from a compositionally distinct parent magma. Like Mantis, Iberia (0.066–0.1) and Davy Crockett (0.079–0.087) also show All_{zpm}/All_{glass} ratios well below equilibrium, confirming they did not crystallize from their surrounding glass. While Iberia had been proposed to originate from a gabbronorite[13], our data do not constrain its source—only that its parent melt was distinct from the impact-generated glass now surrounding it, reinforcing the broader evidence of impact reworking in these breccias. Davy Crockett exhibits the same disequilibrium signature, reinforcing that it was inherited rather than formed from the melt phase now surrounding it. The Crumble Cake zircon follows this trend, with the lowest All_{zpm}/All_{glass} ratio (0.044–0.047) among these samples, confirming that it did not crystallize from the surrounding melt.

In summary, these findings reinforce that matrix zircons were not derived from the melt phase they are now associated with but were instead incorporated as pre-existing crystals, further supporting the widespread impact reworking of lunar breccias. However, beyond simply indicating disequilibrium, the absolute AlI_{zpm} values (Fig. 5) provide insight into the composition of their original parent magma. Our experiments show that higher Al in the melt leads to higher AlI_{zpm} values in zircon. Because impact-generated melts on the Moon typically exhibit elevated Al concentrations (as observed in this study and reported in ref. 31), zircons crystallizing from such melts would be expected to have correspondingly higher AlI_{zpm} values. Instead, the low AlI_{zpm} values observed in these matrix zircons indicate that their parent melts were less enriched in Al, distinguishing them from the impact-generated melts that now surround them. This contrast between zircon and glass compositions enables us to reconstruct original melt chemistry, separating primary magmatic conditions from later impact-related melts, while also serving as a proxy for the parent magma's overall Al/Si ratio. Our approach thus provides a new analytical tool that can access previously lost information about primary magmatic conditions in highly altered samples. Even though impact processes have extensively altered the surrounding melt and glass, AlI_{zpm} preserves a record of the parent melt composition, providing a rare geochemical window into lunar magmatic evolution where primary zircon compositions remain intact, even when the associated glass signatures are no longer pristine.

Crystallographic integrity and Al preservation

To evaluate whether deformation processes influenced the Al content in lunar zircons, we utilized EBSD data reported by Grange et al. [22] for grains from 73235,59 and 73235,60, complemented by our own EBSD analyses (Fig. S12) and existing data from Timms et al. [37]. These combined datasets provide critical insight into whether the Al content reflects the original magmatic compositions or has been affected by impact-induced remobilization.

EBSD data reveal that the Tiger, Cracker, and Hexagon zircons exhibit minimal crystallographic deformation, with misorientation angles between 4° and 6°. Based on established principles of zircon deformation microstructures[38], networks of crystal-plastic deformation connected to grain boundaries can create fast-diffusion pathways for trace element mobility, even along low-angle boundaries. These pathways are typically characterized by systematic changes in cathodoluminescence (CL) spectra and development of new porosity along boundaries. High-resolution EBSD mapping and detailed CL spectroscopy of our analyzed zircons (Figs. S1–6 and S12) show they lack these diagnostic microstructural networks and associated features that would enable enhanced diffusion. Our analyzed zircons show no signs of recrystallization, shock-induced amorphization, or connected networks of high-angle grain boundaries in the regions analyzed. The absence of connected deformation microstructure networks across key domains, confirmed through systematic EBSD mapping at submicron resolution, indicates that deformation processes have not significantly influenced the Al content in these grains. These findings align with Grange et al. [22], who documented minimal deformation in zircons from these samples. Specifically, Grange et al. [22] report that the Tiger zircon exhibits a gradual misorientation of ~4°, interpreted as preserving its magmatic structure. The absence of interconnected crystal-plastic deformation networks, rather than just the low misorientation angle alone, is insufficient to facilitate significant lattice disruption or trace element mobility, as confirmed by consistent U-Pb ages (~ 4354 ± 8 Ma) across the grain. These findings are further supported by the EBSD data presented by Timms et al. [37] in their systematic mapping of deformation microstructures in these grains, which documented minimal crystallographic distortion in these domains. Similarly, the Hexagon zircon shows cumulative misorientations well below 6°, with detailed CL and EBSD mapping showing preserved magmatic growth zoning without modification of primary growth features that would indicate element mobility along deformation pathways (Figs. S6 and S12). These observations align with Timms et al. [37], who documented that this grain shows no variations in EBSD pattern quality and exhibits minimal (< 5°) crystallographic orientation variations, further confirming its preservation of primary magmatic features. The Cracker zircon is more complex, as it exhibits pronounced fragmentation, with fragments misoriented relative to each other by up to 40°. However, EBSD mapping shows that the individual fragments remain internally homogeneous, with misorientation angles within each fragment consistently below 6° (Grange et al.[22]; this study). This observation is further supported by Timms et al.[37], who also documented that while the grain shows a network of brittle fractures with significant rotation between fragments, the individual fragments preserve their internal crystallographic integrity. Importantly, high-resolution EBSD mapping of these fragments shows no evidence of the interconnected deformation microstructure networks that Timms et al. [38] identified as critical for enabling element mobility. This pattern suggests that the observed structure results from mechanical damage rather than shock-induced chemical or isotopic effects. Importantly, we specifically targeted minimally deformed regions (< 4° misorientation) that our detailed microstructural analysis confirmed were free of connected deformation networks for SIMS analyses, ensuring that the measured Al concentrations reflect primary magmatic conditions. The higher Al content in Cracker compared to other matrix zircons likely reflects crystallization from a distinct felsic melt, consistent with geochemical characteristics observed in the 14303 clasts. Collectively, the preserved oscillatory zoning, absence of connected deformation microstructure networks (documented through systematic high-resolution EBSD and CL mapping), and lack of shock-induced amorphization in these zircons confirm that Al in their analyzed domains has not experienced significant post-crystallization remobilization. These observations provide robust evidence that the Al content in Tiger, Hexagon, and the targeted regions of Cracker represents the composition of their parent magmatic melts.

For 14303,49, EBSD imaging was not feasible due to the poor condition of the sample. Despite this limitation, Grange et al. [13] conducted detailed microstructural and cathodoluminescence imaging of zircons in 14303,49, including Behemoth (their 14303,49 zircon#1). They interpreted the preservation of distinct oscillatory zoning and the absence of shock-induced microstructures as evidence that the grain retains primary magmatic features. Upon examination of Behemoth in this study, we found no evidence contradicting their observations. The cathodoluminescence imaging revealed well-defined growth zoning, indicative of crystallization in a magmatic environment (Fig. S2). Furthermore, no signs of recrystallization, amorphization, or high-angle grain boundaries were observed, supporting the conclusion that deformation did not significantly influence the zircon's geochemistry (Fig. S2). Based on Grange et al. [13] and our examination, we conclude that the Al content in Behemoth reliably reflects the parent magmatic composition. Collectively, these observations confirm that Al in lunar zircons provides a robust geochemical signature of their parent melt, even for impact-affected samples like 14303,49. This interpretation of primary Al preservation is indirectly supported by recent atom probe tomography studies of lunar zircon. In analyzing zircon from Apollo sample 72255, which experienced a similar impact history to our samples, Greer et al. [39] demonstrated the absence of nanoscale clustering of both Pb and Y atoms in domains dated at ~4.46 Ga, which is even older than the zircons in our study. Given that Pb is a large, highly incompatible element that does not readily substitute into the zircon structure, the demonstrated immobility of Pb at the atomic scale strongly suggests that smaller, more compatible elements like Al would have remained equally or more stable within the crystal structure over time. This preservation of primary element

distributions in older, similarly impact-affected lunar zircons supports our interpretation that the Al contents measured in our samples reflect original magmatic compositions.

These findings demonstrate that the analyzed lunar zircons, even when subjected to impact-related deformation, have not undergone significant Al remobilization, as indicated by the absence of significant lattice distortion and the preservation of original crystallographic orientations[13,22,37,38]. The minimal crystallographic deformation observed in Tiger, Hexagon, and Cracker confirms that post-crystallization processes have not significantly altered Al mobility, while the preserved oscillatory zoning and chemical homogeneity of Behemoth further underscore the robustness of these geochemical signatures, even in samples with mechanical damage. This demonstrates that despite physical deformation, these zircons retain their original Al compositions, reinforcing their reliability as tracers of primary magmatic conditions. Together, the EBSD and microstructural data, supported by careful geochemical analyses, provide compelling evidence that Al in these zircons reliably records the composition of their parent magmatic melts. These results lay a firm foundation for interpreting the magmatic evolution of lunar felsic clasts and breccias, as detailed in the following discussion.

Discussion

Our Al-in-zircon approach provides compelling evidence that both felsic clasts and matrix zircons in lunar breccias are surrounded by impact-generated melts, with no preserved primary igneous signatures in these materials[4,13,14,22,24,31]. However, the zircons themselves retain their original Al compositions, as demonstrated by our textural analyses. These grains likely crystallized from either endogenic lunar magmatic processes or early impact melt sheets before being incorporated as reworked fragments into impact-assembled clastic units/brecciated matrix, preserving evidence of their pre-brecciation crystallization history. Felsic clasts have often been interpreted as remnants of pristine igneous rocks, yet our findings demonstrate far more extensive impact modification than previously recognized. While previous studies, such as those by Grange et al. [13,22], acknowledged shock effects in these zircons but argued for significant underlying igneous characteristics, our data show that only the zircons preserve their original crystallization signatures, with their surroundings are largely overprinted by impact processes. This challenges the fundamental interpretation of these clasts as pristine magmatic material. Similarly, matrix zircons show no geochemical equilibrium with their surrounding impact melt[13,25,36], demonstrating that they are inherited grains rather than products of the melt that now surrounds them. While their current geological context has been extensively reworked by impact processes, these zircons preserve valuable records of their parent magma composition, offering insights into the magmatic conditions that existed before their incorporation into the breccia matrix.

These observations may have broader implications beyond zircon-bearing rocks, extending to non-zircon-bearing lithologies traditionally considered pristine, such as ferroan anorthosites (FANs). Although our study does not directly test FANs, their classification as primary igneous products of the LMO is often based on criteria similar to those used for our zircon-bearing samples. Given our findings on the limitations of these criteria, it is prudent to approach the interpretation of non-zircon-bearing lithologies with caution, as they too could be more extensively influenced by impact processes than previously understood[14,16,17,19–21].Until new geochemical tools tailored specifically to non-zircon-bearing lithologies are developed, it remains essential to consider the possibility that some primary samples might be more altered by impact processes than previously thought. While our findings do not challenge the LMO model itself, they suggest that the state of primary samples used to reconstruct the history of the lunar crust warrants closer examination. This approach should ensure that impact effects are fully accounted for, as demonstrated by our methodology for zircon-bearing lithologies. As we embark on a new era of lunar exploration, our findings underscore the importance of adopting a nuanced approach to unraveling the Moon's complex geological history. The pervasive impact reworking revealed by our study highlights the need for a more refined framework to assess the pristine nature of lunar samples and accurately interpret their igneous origins. Extracting reliable information about the Moon's primary igneous history will require the development of high-resolution geochemical tools, akin to our Al-in-zircon approach for zircon-bearing rocks, but specifically tailored to non-zircon-bearing lithologies like FANs. Targeted sampling of regions distal to major impact basins, including the lunar farside, combined with multi-faceted analyses at the sub-grain scale and the application of these advanced tools, will be crucial for probing the fine-scale complexities, recovering pristine lunar rocks, and accurately reconstructing the Moon's magmatic evolution. By integrating these strategies, we can pave the way for discoveries that have the potential to reshape our understanding of lunar formation and evolution, offering new insights into the early Solar System and guiding the direction of future lunar missions.

Methods

Sample selection and filtering

A total of 194 zircon grains were identified across 11 Apollo thin sections from the Apollo 12, 14, and 17 missions. Of these, 79 zircons were found adjacent to glass-like phases, and 74 were large enough to accommodate two SIMS spots for dating and chemical analysis. After applying selection criteria based on size and proximity to glass, 33 zircons were chosen for further study. These zircons either had space for two SIMS spots or had a previously published age, requiring only one additional SIMS spot for trace element analysis.

Some analyses were affected by uneven sample surfaces, contamination from inclusions, or grain cracks. Some others were excluded due to potential contamination from phase overlap, where analyzed spots intersected non-zircon phases, leading to unreliable data. To ensure the highest data quality, only the cleanest analyses—free from phase mixing—were included in the final dataset. Out of 190 total spot analyses on lunar zircons, 52 data points were deemed clean and contamination-free (see Section C for details on the contamination screening). This included 40 successful Al-in-zircon analyses on 14 zircons across 6 thin sections (out of a total of 118 spot attempts, excluding standards) and 12 U-Pb and Pb-Pb analyses on 10 zircons (out of 72 total spot attempts, excluding standards). The successful samples were 1213,7, 14303,49, 73217,15, 73217,52, 73235,59, and 73235,60. In total, 14 zircons yielded both U-Pb and chemical data from the SIMS session. Complementary EPMA was conducted at ASU on 8 of the 14 grains that had both U-Pb and Al-in-zircon analyses (Sample, this section and details resented in Data S1). These 8 grains either had glass inclusions or were in contact with glass. Out of 132 total lunar glass spot analyses, only 40 were successful due to the glass in the remaining spots being unsuitable for analysis. The unsuitable glass was either intergrown with a silica polymorph, exhibited a symplectic texture, contained a mixture of crystallized phases and remnant glass, or was too small for reliable analysis.

Sample description

12013,7 (Fig. S1)
Mission: Apollo 12
Landing Site: Oceanus Procellarum
Sample Type: Breccia

This breccia exhibits a distinct dichotomy, composed of a grey portion dominated by felsite and a black portion characterized by lithic fragments of noritic rocks interspersed with individual plagioclase crystals. While the grey felsite was previously thought to have crystallized in a singular event[40], recent studies, including

microstructural analysis by Simon et al. [30] reveal a more complex history. These studies show evidence of significant disturbance by shock processes and intermingling with the black portion of the breccia. This sample hosts 45 zircons distributed throughout, but only two were large enough for both U-Pb and Al-in-zircon analyses.

- **Zircon: 12013,7 Z20 – "Mark IV":** This cohesive zircon, found within the grey felsite portion, has been identified as part of a Rare Earth Element-rich impact melt[15,41]. It is hosted within a crystalline matrix and exhibits well-preserved CL zoning (Fig. S1). No glass is present in the immediate vicinity. A detailed mineralogical description of the surrounding context within the grey portion is provided in the main text.
- **Zircon: 12013,7 Z34 – "Faulted Barrel":** This larger zircon, also found within the grey felsite portion, has been identified as part of the same REE-rich impact melt event[15,41]. It is split into two parts and, like Mark IV, is hosted within a crystalline matrix with no glass present in the immediate vicinity (Fig. S1).

14303,49 (Fig. S2)
Mission: Apollo 14
Landing Site: Fra Mauro Highlands
Sample Type: Polymict Breccia

Sample 14303 is classified as a polymict breccia with a wholly crystalline matrix. This matrix contains a variety of components, including lithic fragments, plagioclase, and less common fragments of olivine and pyroxene. Our analysis focused on fragment 49, which hosts a large felsic nodule previously studied by Meyer et al. [2]. This nodule, though severely brecciated, exhibits areas with apparently pristine graphic intergrowth textures, suggesting it preserves primary igneous characteristics[2,9]. While 24 zircons were identified within the matrix, all were too small for our analytical techniques. However, the felsic clast yielded four zircons, three of which were suitable for both U-Pb and Al-in-zircon analyses.

- **Zircon: 14303,49 Z16 – Climber:** Located at the center of the felsic clast, this zircon is partially enveloped by clinopyroxene and is in contact with glass but does not contain any glass inclusions (Figs. 1 and S2). No CL data is available for this zircon.
- **Zircon: 14303,49 Z17 – Behemoth:** This grain was reported as 14303,49 zircon#1 in Grange et al. [13]. Also located at the center of the felsic clast, Behemoth is highly fractured. Cathodoluminescence imaging reveals a homogenous core exhibiting magmatic zoning, surrounded by a heterogeneous, brecciated rim (Figs. 1 and S2). U-Pb dating of this zircon initially yielded a discordant scatter of ages approximating 45 Ma and 90 Ma. However, after excluding analyses from spots overlapping fractures, the remaining data yielded internally consistent weighted mean ages of 4208 ± 8 Ma and 4317 ± 11 Ma, respectively (Grange et al. [13], Fig. 1).
- **Zircon: 14303,49 Z18 – Pick:** Situated in the center of the felsic clast, Pick is highly fractured and contains glass inclusions (Figs. 1 and S2). It is partially enveloped by plagioclase and clinopyroxene. The limited extent of melting resulted in a fine-scale intergrowth of melt and crystals around the zircon, precluding isolation of a pure glass phase for analysis. CL zoning is preserved in this zircon.

73217 (Figs. S3 and S4)
Mission: Apollo 17
Landing Site: Taurus-Littrow Valley

We studied two sections from this sample, 73217,15 and 73217,52. Both are characterized as a calcic-plagioclase-rich micro-breccia, featuring a variety of angular mineral clasts and rare lithic clasts within a fine-grained, partially glassy matrix. The matrix itself is compositionally diverse, ranging from micrometer-sized crushed granules of plagioclase and pyroxene to intergranular patches of glass containing delicate acicular apatite crystals. Subhedral hypersthene crystals rimming melt patches and tiny, elongated hypersthene grains within the granulated matrix suggest that recrystallization followed the initial granulation event[42]. We identified 25 zircons within fragment 15, two of which were suitable for both U-Pb and Al-in-zircon analyses. Fragment 52 yielded 24 zircons, with two also suitable for both analyses.

- **Zircon: 73217,15 Z9 – Davy Crockett:** This needle-like zircon is found within a glassy matrix and exhibits no fractures or glass inclusions. Slight chemical zoning detected by CL is preserved (Fig. S3).
- **Zircon: 73217,15 Z14 – Iberia:** This rounded zircon is situated within a matrix containing both glass and mineral fragments. It displays no fractures or glass inclusions, and no obvious CL zoning is preserved (Figs. 2 and S3).
- **Zircon: 73217,52 Z16 – Crumbled Cake:** This rounded zircon possesses a granular-textured rim and shows no fractures or inclusions. No obvious CL zoning is preserved (Fig. S4).
- **Zircon: 73217,52 Z17 – Mantis:** This grain was reported as 73217,52 zircon#2 in Grange et al. [22,24] This acicular zircon is found within a glassy matrix and is associated with needle-like ilmenite. It exhibits perfect angular terminations with no evidence of resorption (Fig. 2). While it hosts small melt inclusions, they were too small for EPMA. No obvious CL zoning is preserved (Figs. 2 and S4).

73235 (Figs. S5 and S6)
Mission: Apollo 17
Landing Site: South Massif
Sample Type: Fine-grained Clast-Rich Aphanitic Impact Melt Breccia

Sample 73235 is classified as a fine-grained, clast-rich aphanitic impact melt breccia[43,44]. It comprises a dense aphanitic melt groundmass with a seriate clast distribution[44]. The groundmass consists of plagioclase, pyroxene, opaque minerals, and rare spinel. Lithic clasts are primarily highland rock types, such as shocked Mg-suite anorthosites and cataclased troctolites and norites, which appear as schlieren within the matrix. Notably, mare basalt clasts are absent[45]. We identified 14 zircons in fragment 59, with only one suitable for both U-Pb and Al-in-zircon analyses. Fragment 60 yielded six zircons, four of which were large enough for both analyses.

- **Zircon: 73235,59 Z1 – Tiger:** This grain was reported as 73235,59#3 in Grange et al. [22]. This zircon exhibits two small zones along its border that appear brighter in CL imaging[13] (Figs. 2 and S5). These zones are significantly younger than the bulk of the grain and have lower U and Th contents, as well as lower Th/U ratios. Tiger also displays two sets of planar features visible in cross-polarized light and as low EBSD pattern quality features in EBSD maps. These features cut through both the bright CL domains and the weakly deformed main part of the grain, indicating a later formation[22].
- **Zircon: 73235,60 Z1 – Oldy:** This grain was reported as 73235,60#3 in Grange et al. [22]. This rounded zircon is situated in a matrix devoid of glass in its immediate vicinity. It exhibits no fractures, glass inclusions, or obvious CL zoning (Fig. S6).
- **Zircon: 73235,60 Z2 – Cracker:** This grain was reported as 73235,60#5 in Grange et al. [22]. This zircon is entirely enclosed within a rock fragment described as a "small granophyric clast of silica and ternary feldspar," interpreted as crystallizing from a felsic melt[2] (Figs. 2 and S6). Cracker displays variations in polishing relief and EBSD pattern quality, indicating several irregular domains of low crystallinity[22]. Brittle fractures fragment the grain, some with measurable offsets. Patchy CL zoning is preserved (Figs. 2 and S6).
- **Zircon: 73235,60 Z3 – Hexagon:** This grain was reported as 73235,60#4 in Grange et al. [22]. This solitary mineral clast is embedded in the breccia matrix (plagioclase and pyroxene, no glass) and exhibits radiating cracks. However, it is

otherwise simple, lacking inclusions, fractures, and CL zoning (Figs. 2 and S6).

- **Zircon: 73235,60 Z6 – Yak:** This grain was reported as 73235,60#2 in Grange et al. [22]. This small, rounded zircon grain is found within a matrix composed of plagioclase and pyroxene (no glass). It displays no inclusions or fractures, and no CL zoning is observed (Fig. S6).

Zircon/glass correlation

Figure 3 in the main manuscript compares AlI_{zpm} and AlI_{glass} values to investigate potential relationships between these parameters. Here we explain how we performed the analyses grouping to evaluate whether these parameters show systematic relationships. Pick, Davy Crockett and Crumble Cake are straight forward as they only hold one Al-in-zircon spot that we compared against any available glass analysis for each zircon (either touching of inclusions). Figure S7 and Data S4 show the details of the correlation for samples having more than one Al-in-zircon spot.

Sample characterization and imaging

Polished thick sections (~100 μm) and standard thin sections were prepared for petrographic analysis. Zircon identification within each sample was conducted using a Field Emission Equipped Microprobe (JXA-8530F) at the LeRoy Eyring Center for Solid State Science, Arizona State University. Element mapping of Zr concentrations was employed for this purpose. An accelerating voltage of 15 kV and a beam current of 20 nA were used for all samples. Cathodoluminescence imaging was performed using a UCLA Tescan SEM equipped with a polychromatic CL detector. Backscattered electron images were acquired using the microprobe (Figs. 1, 2 and Figs. S1–S6), along with reflected light images, to guide spot locations for subsequent ion microprobe analysis.

EBSD analyses were performed on selected zircons from 73235,59 and 73235,60 to assess deformation levels and their potential influence on trace element mobility. These analyses were conducted using the Zeiss Auriga SEM/FIB system at the LeRoy Eyring Center for Solid State Science at Arizona State University. This system is equipped with a high-resolution field emission scanning electron microscope (FE-SEM) and an EBSD detector, capable of generating high-quality crystallographic data. Grains were mapped to quantify cumulative misorientation, identify subgrain boundaries, and detect recrystallized zones. Figure S12 shows EBSD maps for "Hexagon" and "Cracker," overlaid with SIMS analytical spots. Misorientation angles remained below 6° across all analyzed regions, confirming structural preservation consistent with magmatic crystallization. No evidence of amorphous domains, high-angle grain boundaries, or recrystallization features was observed, further supporting the interpretation of Al immobility. These EBSD analyses complement existing microstructural data from Grange et al. [22] and Timms et al. [37], who also documented minimal deformation in zircons from these samples. Grange et al. [22] provided foundational observations, and our work builds on their conclusions by directly linking crystallographic integrity with trace element analyses in regions specifically targeted for SIMS measurements.

Given the importance of zircons from the 14303,49 section to the conclusions of this study, we screened the literature for existing EBSD data on these grains. Grange et al. [13], who conducted a detailed and exhaustive study of Apollo zircons, did not report EBSD data for the large zircon they named 14303,49 Zircon#1 (referred to in this study as "Behemoth"), marking its EBSD status as "NA" in their tables. To fill this gap, we attempted to acquire our own EBSD data for zircons from this section. Upon initial examination, the section's condition presented significant challenges. The epoxy/glue used in mounting the sample was peeling away, compromising the section's structural integrity. EBSD imaging requires a thoroughly polished surface to yield interpretable deformation data. However, during polishing attempts, the section began to deteriorate, with grains and rock fragments visibly peeling away along with the epoxy. Further polishing risked destroying portions of the sample, making it infeasible to continue using standard preparation techniques. We subsequently attempted gentler, manual polishing methods to preserve the sample's integrity while improving surface quality. Despite these efforts, the surface remained inadequate for generating reliable EBSD results. Considering NASA's strict curation policies for minimally destructive analyses, we concluded that EBSD imaging for the 14303,49 section was not feasible. It is likely that Grange et al. [13] reached a similar conclusion during their work on this section. In the absence of EBSD data for "Behemoth" and other zircons from 14303,49, our interpretations rely on other structural observations, including cathodoluminescence imaging and the comprehensive contextual data provided by Grange et al. [13]. These observations support the preservation of primary magmatic features in "Behemoth" and ensure that the zircon's geochemical signatures remain robust for interpretation.

Ion microprobe (SIMS) analyses

Lunar thin sections were plasma cleaned then sonicated in DI H_2O with five minutes spent in ethanol to clean the surface and prepare for a fresh C-coat. At ASU, we applied ~25 nm carbon coat to prevent charging on the sample surface. After sample preparation, they were placed under vacuum at UCLA overnight to promote degassing of the epoxy portion of the sample. Both U-Pb dating, and Al (+ other trace elements) analyses were performed on the UCLA CAMECA ims1290 using the Hyperion-II ion source producing an oxygen ion beam with very low energy dispersion, leading to significantly higher beam brightness and thus smaller diameter beam spots (for a given current) compared to regular duoplasmatron ion source[46].

Samples were measured for U-Pb age using the CAMECA ims1290 ion microprobe at UCLA, with a protocol slightly modified from that of Quidelleur et al. [47] as presented in Barboni et al. [48]. After ultrasonication in deionized water and ethanol, samples were carbon coated. Analyses were made in monocollection mode with a 2 nA O^- beam focused to a ~8 μm spot and accelerated by −13kV to a sample stage held at +10 kV. A 90 second presputter with additional 5 μm raster was used to clean common Pb from the analytical surface before data collection. The mass-resolving power (MRP) was ~5000 to resolve all interferences, most notably those on the various Pb isotopes. Oxygen flooding to 1–2 × 10−5 torr was used to enhance Pb ionization. Correction of the Pb/U relative sensitivity factor was accomplished using the linear correlation between $^{238}UO_2^+/^{238}U^+$ and $^{206}Pb^+/^{238}U^+$ for standard zircons from the standard zircons AS3 and FC1 from Duluth Complex[49]. Common Pb corrections were made using measured ^{204}Pb. We note that because all analyses are >97% radiogenic (and most >99%), variation in common Pb compositions has minor effect on the Pb-Pb ages. We assumed an origin of common Pb by laboratory contamination and used the composition of southern California environmental lead for correction[50]. Each analysis was run for 20 cycles.

Following U-Pb dating, zircons were measured for Al concentration along with selected other trace elements using the CAMECA ims1290 ion microprobe at UCLA. The analytical protocol is similar to that of Trail et al. [32] but with added trace element species. Analyses were made in monocollection mode with a 3 nA O^{3-} beam focused to a 10 μm spot and accelerated by −13kV to a sample stage held at +10 kV. The MRP was ~5000. Targets were pre-sputtered for 3 min with an added 5 μm raster to remove surface contamination. Masses measured included $^{23}Na+$, $^{24}Mg^+$, $^{27}Al^+$, $^{28}Si^+$, $^{31}P^+$, $^{39}K^+$, $^{40}Ca^+$, $^{49}Ti^+$, $^{56}Fe^+$, $^{177}Hf^{++}$, $^{89}Y^+$, $^{180}Hf^{16}O^+$, $^{232}Th^+$, and $^{238}U^+$. ^{28}Si was measured using an axial faraday cup, while the other masses were measured using the axial electron multiplier. All other elements were normalized to ^{28}Si for correction. Al concentrations were corrected using a synthetic Al-doped zircon standard (described in Trail et al. [28]). Concentrations of Na, Mg, P, K, Ti,

Y, Hf, Th, and O were corrected using the NIST610 standard glass, with the 91500 zircon[51] as secondary standard to monitor the correction scheme. The $^{177}Hf^{++}$ doubly-charged peak was used to correct for a $^{178}Hf^{++}$ interference on ^{89}Y.

We relied on the $^{57}Fe/^{30}Si$ ratio as a proxy for contamination, particularly for monitoring potential Ti contamination from Fe-Ti oxides, which are the most likely source of Ti contamination in our samples. Furthermore, we included $^{96}Zr/^{30}Si$, $^{23}Na/^{30}Si$, $^{39}K/^{30}Si$, and $^{44}Ca/^{30}Si$ ratios as additional indicators of potential analytical overlap between the zircon and its surrounding phases and surface contamination. High $^{96}Zr/^{30}Si$ ratios were used to ensure that the analyses were indeed within the zircon grain. $^{23}Na/^{30}Si$, $^{39}K/^{30}Si$, and $^{44}Ca/^{30}Si$ tracked surface contamination. Each analysis was run for 10 cycles. Trace element data are presented in Data S2. We note that we report U, Th and Th/U values as initial, that is, accounting for the change in composition of the radiogenic analytes. Therefore, we back calculate their compositions at the point of the calculated age of the zircon grain.

Importantly, data from zircon analyses that exhibited overlap with non-zircon phases were excluded from the final analysis, as this contamination could distort the true chemical signature of the melt inclusions. This rigorous contamination screening ensured that only the cleanest and most representative data were included in the results, minimizing the risk of phase mixing. The supplementary materials include updated visual highlights of the regions excluded due to contamination.

Glass electron microprobe analyses

We used the Arizona State University JEOL JXA-8530F field emission electron microprobe to analyze interstitial glass compositions in Apollo samples. To acquire data, we utilized the Probe for EPMA software by Probe Software, Inc. Using an accelerating voltage of 15 keV, a probe current of 15 nA and a probe diameter of 5 and 10 μm, we measured the intensities of the Kα lines of Si, Ti, Al, Cr, Fe, Mn, Mg, Ca, Na, and K. We selected counting times of 30 s on the peaks and a combined 30 s on the backgrounds and traced element mobility of Na and K with the time-resolved intensity correction of the Probe for EPMA software. Our analyses did not show consistent decreases of X-ray counts for Na and K, suggesting that no corrections for element mobility were necessary. We used the following standards for the calibration of the electron microprobe: Al and Ca-Anorthite, Cr-Chromite, Fe-Fayalite, Mn-Rhodonite, Mg-Hypersthene, Na-Albite, and K-Orthoclase. Our calibration yielded the following detection limits: 0.01 wt% for Si, Al, Mg, and Na; 0.02 wt% for Ti and Cr; 0.04 wt% for Mn; 0.05 for Fe; and 0.06 for Ca and K. Molar $Al_2O_3^{0.5}/SiO_2$ (AlI_{glass}) was calculated for each glass analysis using the SiO_2 and $Al2O_3$ reported values (Fig. S8 and Data S3). AlI_{glass} $(Al_2O_3)^{0.5}/SiO_2$ by mole ratios were calculated using non-normalized molar values derived from the weight percentages of SiO_2 and Al_2O_3. The moles of SiO_2 and Al_2O_3 were obtained by dividing the wt.% of each oxide by their respective molar masses (60.09 g/mol for SiO_2 and 101.96 g/mol for Al_2O_3). Moles of aluminum were calculated as 2 times the mole of Al, reflecting the stoichiometry of Al_2O_3. This approach does not involve normalization to total moles, as the ratio inherently reflects the proportional relationship between Al and Si. To facilitate reproducibility, Data S8 provides an automated tool for calculating AlI_{glass} values from glass wt.% of Al_2O_3 and SiO_2, ensuring consistent application of these parameters.

Al-in-zircon experiments

We selected 5 starting compositions that capture a range of plausible physical and chemical magma processes on the Moon, including impact-generated melts, immiscible melt generation, and melt mixing. Our first composition (1) is modeled after KREEP basalt 15386, which is thought to have formed from re-melting or assimilation of a late-stage, urKREEP-like LMO residual[45]. This composition is ideal for our purpose because it is interpreted to be an endogenously produced igneous material[45]. It is relic free, has preserved igneous textures, and does not have high siderophile element abundances and is thus considered to be generally free of exogenous input[45]. Importantly, the relatively pristine nature of this composition has led others to conduct experiments to evaluate melt composition evolution along the liquid line of descent, with resulted in liquid immiscibility at *ca.* 1050 °C[52]. The evolved immiscible felsic liquid reported in Hess et al. [52] is expected to saturate in zircon[53,54]. The $Al_2O_3^{0.5}/SiO_2$ (by mole)—i.e., AlI_{glass}—of the starting composition is 0.45. For composition (2) we use results from Roedder and Weiblen[55] who reported the composition of 6 immiscible granitic melt inclusions from 14310,5 This composition is meant to represent another fractionated late-stage residual melt with endogenous origins. This is our most silicic melt composition and is representative of lunar granitic material, for which there are reports of a couple dozen occurrences[4,56]. Evidence for the abundance of this rock type is also reinforced by the remote sensing identification of non-mare silica-rich volcanic constructs on the lunar surface[57]. This also represents the rock mix with the lowest AlI_{glass} which is equal to 0.27. For composition (3) we select a composition analogous to a quartz monzodiorite (QMD) clast 14141,7069 reported in Jolliff[58], which is also nearly identical to QMD clast data reported from 15405 by Taylor[59]. Meyer et al. [2] documented zircon grains in two QMD clasts (15405,57 and 15405,145) found in a lunar breccia. Additionally, the sample they described shares the same mineralogy as a QMD clast examined by Ryder[60] [15405,12]. These samples, characterized by their very high Fe content, are believed to be the result of fractionated basalts, as suggested by Jolliff[58]. Rock composition (4) is a mixture of highland basalt and immiscible granite 14310,5 presented in (2), in 80/20 proportions, respectively. Rutherford et al. [61] proposed this mixture as a potential explanation for the composition observed in certain impact melt breccias. Similarly, Ryder and Bower[62] reported a composition in sample 14064 that aligns with this mixture, indicating its resemblance to melt breccias. This also represents the rock mix with the highest AlI_{glass}, which is equal to 0.55.

And finally, we select a monzonite rock type for composition (5), (AlI_{glass} = 0.37) which are not as common as glasses and crystalline material with granitic composition. Previously, high-temperature experiments were conducted to investigate the origins of these rocks, leading to the conclusion that they are probably not liquids derived from residual fractionated lunar basalts. Rather, they are inferred to be mixtures comprising granitic liquid, plagioclase, and pyroxene cumulates. This suggests they embody various rock types formed through secondary processes on the Moon[61]. Additionally, Lovering and Wark[63] reported the average composition of "monzonites" from multiple clasts across different Apollo missions.

The five target rock composition are provided in Data S5 with AlI_{glass} target compositions between 0.27 to 0.55. These compositions represent a complementary range of primary and secondary magmatic processes. It is also important to keep in mind that lunar impact breccias are produced by at least one impact and are thus a mixture of materials derived from different materials and locations. We do not need to produce the exact melt composition for the project to be successful. Our strategy, rather, is to parameterize ppm Al in zircon as function of AlI_{glass} derived from the experimental product. The application of this parameterization, based on zircon Al content, yields AlI_{zpm}.

Based on the compositions in Supplementary Data 5, we prepared rock mixes in the SiO_2-Al_2O_3-FeO-MgO-CaO-Na_2O-K_2O-ZrO_2 system (±H_2O), following the general strategy outlined in Wang and Trail[27] that we summarize here. First, major oxide mixtures were prepared from reagent grade SiO_2, Al_2O_3, decarbonated $CaCO_3$, $MgCO_3$, Na_2CO_3, and K_2CO_3 to yield a haplobasaltic composition, along with ~5 wt% ZrO_2. Components were ground under ethanol for 30 min in an agate

mortar, dried, and then packed in to a Pt crucible. The mixtures were decarbonated at 850 °C overnight in a muffle furnace. The decarbonated rock mixtures were re-ground (by hand) for 30 min under ethanol before re-packing into a Pt crucible. Rock mixes were heated above the liquidus in a 1 atm furnace for 6 h. This glass was then ground to powder by hand for 1 h under ethanol in a mortar and pestle in preparation for the partitioning experiments[27,29,54,64]. Finally, FeO, additional SiO_2 and $Al(OH)_3$ were added to make the desired rock mix composition.

The experiments were designed to be water-bearing (~ 3 wt %H_2O) for three reasons. First, H^+ is a possible charge balancing reaction for the entry of Al^{3+} in the zircon structure[28,29], second trace H_2O has been documented in lunar samples, and third, H_2O depolymerizes silicate melts, resulting faster diffusivities for Zr and therefore zircons that are of analyzable size under laboratory durations. Rock mixtures were loaded into machined Fe or Pt/Au-Pd capsules and experiments were conducted in a piston cylinder device following the method of Wang and Trail[27]. Briefly, samples were pressurized to 1 GPa, ramped at 200°/min to the desired T (between 1300 and 1050 °C), and left to dwell for 94 to 456 h (Data S7).

Additional rock mixes—an anhydrous suite—where also made from the base mix without the addition of hydrous phases, though these were rarely used due to difficulties with growth zircon in water free systems at laboratory timescales. With these mixes, we conducted 2 successful experiments using melt composition (1) at 1 atmosphere and 1200/1250 °C. Samples were packed into a graphite capsule sealed in an evacuated silica tube, and left to dwell for 24–70 h, and then quenched in a beaker of water. Other attempts were made to synthesize analyzable zircons using the other melt compositions; however, these attempts were unsuccessful.

The Al content of experimental zircon was determined using a Teledyne Cetac (formerly Photon Machines) 193 nm G2 excimer laser ablation (LA) system, coupled with an Agilent 7900 quadrupole inductively coupled plasma mass spectrometer (ICP-MS) at the University of Rochester. The LA system features a HelEx sample chamber, enabling the transport of targeted material to the ICP-MS post-ablation. Helium flow rates in the HelEx sample chamber (MFC1) and the HelEx arm (MFC2) were set at 0.6 L/min and 0.2 L/min, respectively. Additionally, Argon (Ar) was introduced as a carrier gas at 1.3 L/min before a sample was introduced into the plasma. Each analysis comprised a sequence of a 20 s background counts collection, followed by a 15 s LA period, and ended with a 35 s washout period to purge the previous sample and transition to the next. The experimental zircon crystals were analyzed with the laser operating at a fluence of 4.72 J/cm^2 for 15 s with a repetition rate of 10 Hz. Considering that the size of the experimental zircon crystals correlates strongly with the temperature and duration of the experiment, the spot size was selected as 2, 3, or 4 μm, depending on the crystal size. For the analyses with 3 and 4 μm spot sizes, the elements ^{23}Na, ^{27}Al, ^{29}Si, ^{31}P, ^{91}Zr, ^{175}Lu, and ^{178}Hf were examined. Analyses with a 2 μm spot size focused solely on the elements ^{23}Na, ^{27}Al, ^{29}Si, and ^{91}Zr. In analyses using the 2 μm spot size, the number of measured masses was reduced to increase the counting time on the crucial elements. This adjustment aimed to mitigate potential concerns about data precision due to the lower volume of ablated material, ensuring a more robust and accurate analysis within the limitations of the 2 μm spot size.

During analyses, ^{23}Na was treated as a marker element to differentiate between zircon and glass since the ablation process often penetrated through the zircon to the embedded glass. The point at which the laser transitioned from ablating zircon to sampling the glass was carefully monitored in the ^{23}Na spectrum, marked by a sharp increase in counts corresponding to the glass. For elemental compositions, calibrations were performed using a synthetic Al zircon standard reported in Trail et al. [28], the composition of which been documented in Trail et al. [28,32]. We also used a separate Al in zircon standard 'Z_AlPLuHf', synthesized in a piston cylinder using the method described in Trail et al. [29]. Zircon composition data were reduced and calibrated into concentration values using the Iolite 4.1 software package, using the Data Reduction Schemes of Trace Element Next[65], with ^{29}Si used as an internal standard. To assess data quality, glass standards NIST610 and NIST612 were employed as secondary reference materials.

The elemental compositions of the experimental glass were determined using the Cameca SXFive electron probe microanalyzer (EPMA) at Syracuse University, with a 15 kV accelerating voltage for all quantitative measurements. Reference materials applied to unknown samples for calibration were analyzed with a focused 20 nA beam current. These reference materials were also measured as unknowns using the same beam condition to monitor data quality. The experimental glass was examined utilizing a defocused 10 nA beam current with a 10-micron spot size to mitigate potential Na mobility/loss inherent in targeted glasses. Standards of basalt glasses VG2 & A99 were included in the analysis session and were measured using the same beam condition to ensure data quality. The Si values from basalt glass standards obtained with a 10 nA beam current were slightly lower, while measurements at a 20 nA beam current showed values closer to reference material values, which may be attributed to signal loss under lower current conditions.

Each measurement of Al, Si, Na, Mg, Fe, Mn, Al, Si, Na, Mg, Fe, and Mn involved a 20-s peak and 10-s background, while Ti, P, K, and Ca measurements comprised a 10-s peak and 5-s background. The X-ray line applied for Al, Si, Na, Mg, Ti, P, K, Ca, Fe, and Mn elements was Kα, while for Zr, it was Lα. Concentration calibration for each element was accomplished using different reference materials: Sillimanite for Al, basalt glass VG-2, basalt glass A-99, quartz, and Diopside for Si, Jadeite for Na, Enstatite for Mg, Rutile for Ti, Apatite for P, Sanidine for K, Diopside for Ca, Fayalite for Fe, Rhodonite for Mn, and zircon for Zr.

All data and fit results are reported in Data S6 and S7. Several attempts were made to fit the data to various melt parameters. This also included the ASI parameter or ASI (a molar ratio of Al_2O_3/(CaO-Na_2O-K_2O) which is common among terrestrial melts. We initially targeted this melt parameter because it has been used with success for terrestrial samples[27,28]. For instance, Trail et al. [28] measured Al concentration in zircon from 19 geographically and petrologically varied terrestrial rocks. Zircon from peraluminous rocks (ASI ranging from 1.03 to 1.6) exhibited Al in zircon values approximately an order of magnitude higher than those in zircon from metaluminous rocks (ASI between 0.88 and 0.99). This result was confirmed by experiments where the ASI was varied from 0.5 to 1.2[27]. However, the starting rock mix in these experiments only had an SiO_2 content ranging only from 63 to 66 wt% and lacked FeO and MgO, which are two key components in lunar melts. To better reflect the range of probable crystallization environments, our starting lunar compositions ranged from 51 wt% to 76 wt%, (Data S5) and we found that the SiO_2 and Al_2O_3 content of the melt both influence the uptake of Al in zircon.

In considering Al in zircon in a lunar setting we start with the following model reaction after Trail et al. [32]

$$\mathrm{ZrSiO_4(zircon) + 1/2Al_2O_3(melt) + 1/2H_2O(melt) = Zr[AlH]O_4(zircon) + SiO_2(melt)} \quad (1)$$

The equilibrium constant becomes:

$$K = \frac{\left[a^{\mathrm{zrc}}_{\mathrm{Zr[AlH]O4}}\right] \times \left[a^{\mathrm{melt}}_{\mathrm{SiO2}}\right]}{\left[a^{\mathrm{melt}}_{\mathrm{Al2O3}}\right]^{1/2} \times \left[a^{\mathrm{melt}}_{\mathrm{H2O}}\right]^{1/2}} \quad (2)$$

where $a^{\mathrm{melt}}_{\mathrm{Al2O3}}$ is the activity of alumina in the melt, etc. Hereafter we do not directly consider the role of H_2O and assume that it is constant. Note that we have previously established that there is a correlation

between H content (i.e., 'OH') and Al in zircon[29] in hydrothermal fluid-saturated experimental environments. However, we document incorporation of Al into the zircon structure under anhydrous conditions and so there is no evidence that the activity of H_2O in the experimental system is a crucial main driver that controls Al incorporation into the zircon structure. We also assume that:

$$a^{zrc}_{Zr[AlH]O4} \approx [X^{Zrc}_{Al}, \text{ppm}] \times k_1 \quad (3)$$

where k_1 is the Henry's Law constant that relates $a^{Zrc}_{Zr[AlH]O4}$ to $X^{Zrc}_{zr[AlH]O4}$ and the factor that converts $X^{Zrc}_{Zr[AlH]O4}$ to X^{Zrc}_{Al} (in ppm). We make similar assumptions for the melt composition assuming there a constant of proportionality that relates the activity of melt components Al_2O_3 and SiO_2 to their respective mole fractions. Taking all this into consideration and rearranging, we can express the following proportionality:

$$\text{Al } \textit{in zircon} \text{ (ppm)} \propto \frac{\left([Al_2O_3]_{melt}\right)^{1/2}}{[SiO_2]_{melt}} = \text{AlI}_{zpm} \quad (4)$$

where the values of the melt composition represented as molar quantities. This predicts that as $[Al_2O_3]_{melt}$ increases, so should the ppm Al in zircon. It also predicts that an increase in $[SiO_2]_{melt}$ will yield a corresponding decrease of Al concentration in zircon. This simple model is broadly confirmed with our experimental data (Fig. S9). We use the basic form of Eq. 4 to fit the data, where results of these fits are summarized in Data S6.

Several analyses yield totals falling well below 95%, particularly at lower temperatures. While we primarily attribute these low totals to fractional crystallization, which increases the water content and reduces the measured oxide totals, we acknowledge that unmeasured noble metals (Pt, Au, Pd) from the experimental capsules may also contribute to these deficits. In the interest of transparency and scientific reproducibility, we chose to include these lower-total analyses in the final calibration. All experimental samples are preserved and available for future analytical work. For reference, filtering out analyses with totals below 95% increases the best-fit slope from approximately ~600 to ~850; using this larger slope would only exacerbate the discrepancy between AlI_{glass} and AlI_{zpm} in the lunar dataset. All the data and the resulting fits can be found in Data S6 and S7.

We also note that MnO sometimes present in the silicate glass analyses in minor amounts. MnO is also commonly found as a minor component in natural samples; for example, sample 15386 used in designing our rock mixture—contains ~0.15 wt% MnO. Although MnO was not deliberately added to our starting materials, we analyzed for it because industrially processed—Fe used in some of our capsules may have Mn as an impurity. In experiments where the melt was in direct contact with Fe capsules, the MnO content averaged ~0.3 wt% across all temperatures (e.g., 0.28 wt% at 1100 °C). In contrast, when Pt capsules were placed between the melt and the Fe, MnO contents averaged ~0.01 wt%. Nevertheless, in cases where MnO is detected, it is similar to the concentration found in natural samples.

These experimental glass results ($Al_2O_3^{0.5}/SiO_2$ (by mole))– along with Al contents in zircon are used to estimate AlI_{zpm} lunar zircon host melts, which are compared to actual AlI_{glass} of lunar glass proximal to the zircon (Fig. S10). We chose to force our regression through zero based on the fundamental premise that no Al in the melt should result in no Al in zircon. While a non-zero intercept could suggest a minimum Al content required in the melt for zircon to incorporate Al, we favor the simpler model that assumes direct proportionality. Throughout this study, we use the forced-through-origin regression values for all figures and interpretations. For transparency, both forced and non-forced regression AlI_{zpm} values are provided in Data S6, and we include an auto-calculation tool in Data S8 that allows readers to calculate AlI_{zpm} using either approach for their own Al-in-zircon measurements. Note that over the T range explored, there is no well-defined T trend with the data, and so our fit does not include T as a key variable in these fits (Fig. S9).

Data availability

The data generated in this study are provided in the Supplementary Materials and main text. The literature data used in Fig. 4 were compiled from previously published studies, which are cited in the figure caption. No new datasets requiring repository deposition were generated for this study. All geological samples analyzed in this research are Apollo lunar samples, provided on loan by NASA's Curation and Analysis Planning Team for Extraterrestrial Materials (CAPTEM). These samples were collected during the Apollo 14 and 17 missions and are curated by NASA's Johnson Space Center. Researchers interested in accessing these samples should contact NASA CAPTEM directly to inquire about sample availability and loan procedures.

References

1. Warren, P. H. A concise compilation of petrologic information on possibly pristine non mare Moon rocks. *Am. Mineral.* **78**, 360–376 (1993).
2. Meyer, C., Williams, I. S. & Compston, W. Uranium-lead ages for lunar zircons: evidence for a prolonged period of granophyre formation from 4.32 to 3.88 Ga. *Meteorit. Planet. Sci.* **31**, 370–387 (1996).
3. Borg, L. E., Connelly, J. N., Boyet, M. & Carlson, R. W. Chronological evidence that the Moon is either young or did not have a global magma ocean. *Nature* **477**, 70–72 (2011).
4. Seddio, S. M., Jolliff, B. L., Korotev, R. L. & Zeigler, R. A. Petrology and geochemistry of lunar granite 12032,366-19 and implications for lunar granite petrogenesis. *Am. Miner.* **98**, 1697–1713 (2013).
5. Zeng, X. et al. New evidence for 4.32 Ga ancient silicic volcanism on the moon. *Geophys. Res. Lett.* **48**, e2021GL092639 (2021).
6. Valencia, S. N., Korotev, R. L. & Jolliff, B. L. Compositional analysis of Apollo 12 Granitic Breccia 12013: insights into protoliths and formation. *Geochim. Cosmochim. Acta* **367**, 189–212 (2024).
7. Warren, P. H., Jerde, E. A. & Kallemeyn, G. W. Lunar meteorites: siderophile element contents, and implications for the composition and origin of the Moon. *Earth Planet. Sci. Lett.* **91**, 245–260 (1989).
8. Warren, P. H., Jerde, E. A. & Kallemeyn, G. W. Pristine Moon rocks: a "large" felsite and a metal-rich ferroan anorthosite. *J. Geophys. Res.: Solid Earth* **92**, E303–E313 (1987).
9. Warren, P. H., Taylor, G. J. & Keil, K. Regolith breccia allan hills A81005: evidence of lunar origin, and petrography of pristine and nonpristine clasts. *Geophys. Res. Lett.* **10**, 779–782 (1983).
10. Shervais, J. W., Lawrence, A. & Taylor, J. Ancient crustal components in the Fra Mauro breccias. *J. Geophys. Res.* **88**, B177–B192 (1983).
11. Norman, M. D. & Ryder, G. A Summary of the Petrology and Geochemistry of Pristine Highlands Rocks. in *Proceedings of the Tenth Lunar and Planetary Science Conference*, Vol. 1 (ed. Merrill, R. B.) 531–559 (Pergamon Press, New York, 1979).
12. Ryder, G. & Score, R. The distinction of pristine from meteorite-contaminated highlands rocks using metal compositions. in *Proceedings of the Eleventh Lunar and Planetary Science Conference*, Vol. 1 (ed. Merrill, R. B.) 471–479 (Pergamon Press, New York, 1980).
13. Grange, M. L., Pidgeon, R. T., Nemchin, A. A., Timms, N. E. & Meyer, C. Interpreting U–Pb data from primary and secondary features in lunar zircon. *Geochim. Cosmochim. Acta* **101**, 112–132 (2013).
14. Pernet-Fisher, J. F., Joy, K. H., Martin, D. J. P. & Hanna, K. L. D. Assessing the shock state of the lunar highlands: implications for the petrogenesis and chronology of crustal anorthosites. *Sci. Rep.* **7**, 5888 (2017).

15. Thiessen, F., Nemchin, A. A., Snape, J. F., Bellucci, J. J. & Whitehouse, M. J. Apollo 12 breccia 12013: impact-induced partial Pb loss in zircon and its implications for lunar geochronology. *Geochim. Cosmochim. Acta* **230**, 94–111 (2018).
16. Gross, J., Treiman, A. H. & Mercer, C. N. Lunar feldspathic meteorites: constraints on the geology of the lunar highlands, and the origin of the lunar crust. *Earth Planet. Sci. Lett.* **388**, 318–328 (2014).
17. Russell, S. S., Joy, K. H., Jeffries, T. E., Consolmagno, G. J. & Kearsley, A. Heterogeneity in lunar anorthosite meteorites: implications for the lunar magma ocean model. *Philos. Trans. R. Soc. A: Math., Phys. Eng. Sci.* **372**, 20130241 (2014).
18. Boyet, M., Carlson, R. W., Borg, L. E. & Horan, M. Sm–Nd systematics of lunar ferroan anorthositic suite rocks: constraints on lunar crust formation. *Geochim. Cosmochim. Acta* **148**, 203–218 (2015).
19. Borg, L. E. et al. Isotopic evidence for a young lunar magma ocean. *Earth Planet. Sci. Lett.* **523**, 115706 (2019).
20. Borg, L. E. & Carlson, R. W. The evolving chronology of moon formation. *Annu. Rev. Earth Planet. Sci.* **51**, 25–52 (2022).
21. Torcivia, M. A. & Neal, C. R. Unraveling the components within apollo 16 ferroan anorthosite suite cataclastic anorthosite sample 60025: implications for the lunar magma ocean model. *J. Geophys. Res.: Planets* **127**, (2022).
22. Grange, M. L., Nemchin, A. A., Timms, N., Pidgeon, R. T. & Meyer, C. Complex magmatic and impact history prior to 4.1Ga recorded in zircon from Apollo 17 South Massif aphanitic breccia 73235. *Geochim. Cosmochim. Acta* **75**, 2213–2232 (2011).
23. Nemchin, A. A., Grange, M. L., Pidgeon, R. T. & Meyer, C. Lunar zirconology. *Aust. J. Earth Sci.* **59**, 277–290 (2012).
24. Grange, M. L. et al. Thermal history recorded by the Apollo 17 impact melt breccia 73217. *Geochim. Cosmochim. Acta* **73**, 3093–3107 (2009).
25. Nemchin, A. et al. Timing of crystallization of the lunar magma ocean constrained by the oldest zircon. *Nat. Geosci.* **2**, 133–136 (2009).
26. Grange, M. L., Nemchin, A. A. & Pidgeon, R. T. The effect of 1.9 and 1.4 Ga impact events on 4.3 Ga zircon and phosphate from an Apollo 15 melt breccia. *J. Geophys. Res.: Planets* **118**, 2180–2197 (2013).
27. Wang, Y. & Trail, D. Aluminum partitioning between zircon and haplogranitic melts: the influence of temperature and melt composition. *Chem. Geol.* **511**, 71–80 (2019).
28. Trail, D., Tailby, N., Wang, Y., Harrison, T. M. & Boehnke, P. Aluminum in zircon as evidence for peraluminous and metaluminous melts from the Hadean to present. *Geochem. Geophys. Geosyst.* **18**, 1580–1593 (2017).
29. Trail, D., Thomas, J. B. & Watson, E. B. The incorporation of hydroxyl into zircon. *Am. Miner.* **96**, 60–67 (2011).
30. Simon, J. I. et al. Volatiles in lunar felsite clasts: impact-related delivery of hydrous material to an ancient dry lunar crust. *Geochim. Cosmochim. Acta* **276**, 299–326 (2020).
31. Crow, C. A. et al. Impact origin of lunar zircon melt inclusions in apollo impact melt breccia 14311. *Meteorit. Planet. Sci*. https://doi.org/10.1111/maps.14162 (2024).
32. Trail, D., Barboni, M. & McKeegan, K. D. Evidence for diverse lunar melt compositions and mixing of the pre-3.9 Ga crust from zircon chemistry. *Geochimica et. Cosmochimica Acta* **284**, 173–195 (2020).
33. Davis. *Microstructural Geochronology of Zircon Across the Central Uplift.pdf*. (Ontario, Canada: Western University, 2016).
34. Zhang, B. et al. Imbrium age for zircons in apollo 17 South massif impact melt breccia 73155. *J. Geophys. Res. Planets* **124**, 3205–3218 (2019).
35. Barboni, M. et al. High-precision U-Pb zircon dating identifies a major magmatic event on the Moon at 4.338 Ga. *Sci. Adv.* **10**, eadn9871 (2024).
36. Pidgeon, R. T. et al. Complex history of a zircon aggregate from lunar breccia 73235. *Geochim. Cosmochim. Acta* **71**, 1370–1381 (2007).
37. TIMMS, N. E. et al. Resolution of impact-related microstructures in lunar zircon: a shock-deformation mechanism map. *Meteorit. Planet. Sci.* **47**, 120–141 (2012).
38. Timms, N. E., Reddy, S. M., Gerald, J. D. F., Green, L. & Muhling, J. R. Inclusion-localised crystal-plasticity, dynamic porosity, and fast-diffusion pathway generation in zircon. *J. Struct. Geol.* **35**, 78–89 (2012).
39. Greer, J. et al. 4.46 Ga zircons anchor chronology of lunar magma ocean. *Geochem. Perspect. Lett.* **27**, 49–53 (2023).
40. Quick, J. E., Albee, A. L. & James, O. B. Petrology and petrogenesis of lunar breccias 12013. *Proc. Lunar Planet. Sci. Conf.* **12B**, 117–172 (1981).
41. Quick, J. E., James, O. B. & Albee, A. L. A Reexamination of the Rb-Sr isotopic systematic of lunar breccia 12013. *Proc. Lunar Planet. Sci. Conf.* **12B**, 173–184 (1981). vol.
42. Ishii, T., McCallum, S. & Ghose, S. Petrological and thermal histories of a lunar breccia 73217 as inferred from pyroxene crystallization sequences, exsolution phenomena, and pyroxene geothermometry. *J. Geophys. Res.: Solid Earth* **88**, A631–A644 (1983).
43. Spudis, P. D. & Ryder, G. Apollo 17 impact melts and their relation to the Serenitatis basin. *Proc. Lunar Planet. Sci. Conf.* **12A**, 133–148 (1981). vol.
44. Ryder, G. Catalog of Apollo 17 Rocks, Volume 1: Stations 2 and 3 (South Massif). (eds. Dietrich, J. & Gooding, J.) (NASA Johnson Space Center, Houston, 1993).
45. Warren, P. H. & Wasson, J. T. The compositional-petrographic search for pristine non-mare rocks—third foray. in *Proceedings of the Tenth Lunar and Planetary Science Conference*, Vol. 1 (ed. Merrill, R. B.) 583–610 (Pergamon Press, New York, 1979).
46. Liu, M.-C., McKeegan, K. D., Harrison, T. M., Jarzebinski, G. & Vltava, L. The Hyperion-II radio-frequency oxygen ion source on the UCLA ims1290 ion microprobe: Beam characterization and applications in geochemistry and cosmochemistry. *Int. J. Mass Spectrom.* **424**, 1–9 (2018).
47. Quidelleur, X. et al. Thermal evolution and slip history of the Renbu Zedong Thrust, southeastern Tibet. *J. Geophys. Res.: Solid Earth* **102**, 2659–2679 (1997).
48. Barboni, M., Marquardt, M., Timms, N. E. & Bell, E. A. HED zircons as a window into the solar system's first crust: decoupling primordial differentiation, metamorphism and impact events through textural and chemical studies. *Geochim. Cosmochim. Acta* **376**, 113–133 (2024).
49. Paces, J. B. & Miller, J. D. Precise U-Pb ages of Duluth Complex and related mafic intrusions, northeastern Minnesota: Geochronological insights to physical, petrogenetic, paleomagnetic, and tectonomagmatic processes associated with the 1.1 Ga Midcontinent Rift System. *J. Geophys. Res.: Solid Earth* **98**, 13997–14013 (1993).
50. Sañudo-Wilhelmy, S. A. & Flegal, A. R. Temporal variations in lead concentrations and isotopic composition in the Southern California Bight. *Geochim. Cosmochim. Acta* **58**, 3315–3320 (1994).
51. Wiedenbeck, M. et al. Further characterisation of the 91500 Zircon Crystal. *Geostand. Geoanalytical Res.* **28**, 9–39 (2004).
52. Hess, P. C., Horzempa, P. & Rutherford, M. J. Fractionation of Apollo 15 KREEP basalts. in *Proceedings of the Twentieth Lunar and Planetary Science Conference* (eds. Sharpton, V. L. & Ryder, G.) 408–409 (Lunar and Planetary Institute, Houston, 1989).
53. Dickinson, J. E. & Hess, P. C. Zircon saturation in lunar basalts and granites. *Earth Planet. Sci. Lett.* **57**, 336–344 (1982).
54. Boehnke, P., Watson, E. B., Trail, D., Harrison, T. M. & Schmitt, A. K. Zircon saturation re-revisited. *Chem. Geol.* 1–48 https://doi.org/10.1016/j.chemgeo.2013.05.028 (2013).

55. Roedder, E. & Weiblen, P. W. Petrographic and petrologic features of Apollo 14, 15, and Luna 16 samples. in *Proceedings of the Third Lunar Science Conference*, Vol. 1 (ed. King, E. A. Jr.) 251–279 (MIT Press, Cambridge, 1972).
56. Roedder, E. & Weiblen, P. W. Lunar petrology of silicate melt inclusions, Apollo 11 rocks. in *Proceedings of the Second Lunar Science Conference*, Vol. 1 (ed. Levinson, A. A.) 507–528 (MIT Press, Cambridge, 1971).
57. Hagerty, J. J. et al. Refined thorium abundances for lunar red spots: implications for evolved, nonmare volcanism on the Moon. *J. Geophys. Res.: Planets* **111**, (2006).
58. Jolliff, B. L., Korotev, R. I. & Haskin, L. A. Geochemistry of 2-4-mm particles from Apollo 14 soil (14161) and implications regarding igneous components and soil-forming processes. *Proc. Lunar Planet. Sci. Conf.* **21**, 193–219 (1991).
59. Taylor, S. R. Refractory and moderately volatile element abundances in the Earth, Moon, and meteorites. in *Proceedings of the Eleventh Lunar and Planetary Science Conference*, Vol. 1 (ed. Merrill, R. B.) 333–348 (Pergamon Press, New York, 1980).
60. Ryder, G. Lunar sample 15405: remnant of a KREEP basalt-granite differentiated pluton. *Earth Planet. Sci. Lett.* **29**, 255–268 (1976).
61. Rutherford, M. J., Hess, P. C., Ryerson, F. J., Campbell, H. W. & Dick, P. A. The chemistry, origin, and petrogenetic implications of lunar granite and monzonite. in *Proceedings of the Seventh Lunar Science Conference*, Vol. 1 (ed. Merrill, R. B.) 1723–1740 (Pergamon Press, New York, 1976).
62. Ryder, G. & Bower, J. F. Poikilitic KREEP impact melts in the Apollo 14 white rocks. in *Proceedings of the Seventh Lunar Science Conference*, Vol. 1 (ed. Merrill, R. B.) 1925–1948 (Pergamon Press, New York, 1976).
63. Lovering, J. F. & Wark, D. A. The lunar crust—chemically defined rock groups and their potassium-uranium fractionation. in *Proceedings of the Sixth Lunar Science Conference*, Vol. 1 (ed. Merrill, R. B.) 1203–1217 (Pergamon Press, New York, 1975).
64. Trail, D., Watson, E. B. & Tailby, N. D. Ce and Eu anomalies in zircon as proxies for the oxidation state of magmas. *Geochim. Cosmochim. Acta* **97**, 70–87 (2012).
65. Paton, C., Hellstrom, J., Paul, B., Woodhead, J. & Hergt, J. Iolite: freeware for the visualisation and processing of mass spectrometric data. *J. Anal. At. Spectrom.* **26**, 2508–2518 (2011).
66. Shearer, C. et al. Magmatic evolution II: a new view of post-differentiation magmatism. *Rev. Miner. Geochem.* **89**, 147–206 (2023).
67. Warren, P. H., Taylor, G. J., Keil, K., Shirley, D. N. & Wasson, J. T. Petrology and chemistry of two "large" granite clasts from the moon. *Earth Planet. Sci. Lett.* **64**, 175–185 (1983).
68. Shervais, J. W. & McGee, J. J. Ion and electron microprobe study of troctolites, norite, and anorthosites from Apollo 14: evidence for urKREEP assimilation during petrogenesis of Apollo 14 Mg-suite rocks. *Geochim. Cosmochim. Acta* **62**, 3009–3023 (1998).
69. Zeigler, R. A., Korotev, R. L., Jolliff, B. L., Haskin, L. A. & Floss, C. The geochemistry and provenance of Apollo 16 mafic glasses. *Geochim. Cosmochim. Acta* **70**, 6050–6067 (2006).
70. Delano, J. W. Geochemical comparison of impact glasses from lunar meteorites ALHA81005 and MAC88105 and Apollo 16 regolith 64001. *Geochim. Cosmochim. Acta* **55**, 3019–3029 (1991).
71. Hughes, S. S., Delano, J. W. & Schmitt, R. A. Petrogenetic modeling of 74220 high-Ti orange volcanic glasses and the Apollo 11 and 17 high-Ti mare basalts. In *Lunar and Planetary Science Conference*, 19th, Houston, TX, Mar. 14–18, 1988, Proceedings (A89-36486 15–91). Cambridge/Houston, TX, Cambridge University Press/Lunar and Planetary Institute 19, 1989, 175–188 (1988).
72. Stoeser, D.B., Marvin, U.B., Wood, J.A., Wolfe, R.W. & Bower, J.F. Petrology of a stratified boulder from South Massif, Taurus-Littrow. In *Proceedings Lunar Science Conference, 5th, Houston, Tex.*, March 18–22, 1974, Vol 1. (A75-39540 19–91) 355–377 (Pergamon Press, Inc. New York, 1974).

Acknowledgements

We thank CAPTEM for providing all the Apollo lunar samples presented in this study, which were analyzed under approved sample allocation agreements. We also thank Axel Whittmann for assistance with SEM and EBSD imaging. This research was supported by NASA grant 18-SSW18-0138 to DT and MB. The ion microprobe laboratory at UCLA was partially funded by a grant from NSF's Instrumentation and Facilities Program (2154590).

Author contributions

Conceptualization: M.B., D.T. Methodology: D.T., M.B. Investigation: E.N., M.B., D.T., E.A.B., H.Y.C. Visualization: M.B., E.N. Funding acquisition: D.T., M.B. Project administration: M.B., D.T. Supervision: M.B., D.T. Writing – original draft: M.B., E.N., D.T. Writing – review & editing: M.B., D.T., E.A.B.

Competing interests

The authors declare no competing interests.

Additional information

Supplementary information The online version contains supplementary material available at https://doi.org/10.1038/s41467-025-57691-z.

Correspondence and requests for materials should be addressed to M. Barboni.

Peer review information *Nature Communications* thanks Justin Simon and the other, anonymous, reviewers for their contribution to the peer review of this work. A peer review file is available.